

Analyzing X-Ray tomographies of granular packings

Simon Weis¹ and Matthias Schröter²

¹*Institut für Theoretische Physik I, Friedrich-Alexander-Universität, 91058 Erlangen, Germany*

²*Institute for Multiscale Simulation, Friedrich-Alexander-Universität, 91052 Erlangen, Germany.*

(Dated: 21 March 2017)

Starting from three-dimensional volume data of a granular packing, as e.g. obtained by X-ray Computed Tomography, we discuss methods to first detect the individual particles in the sample and then analyze their properties. This analysis includes the pair correlation function, the volume and shape of the Voronoi cells and the number and type of contacts formed between individual particles. We mainly focus on packings of monodisperse spheres, but we will also comment on other monoschematic particles such as ellipsoids and tetrahedra. This paper is accompanied by a package of free software containing all programs (including source code) and an example three-dimensional dataset which allows the reader to reproduce and modify all examples given.

I. INTRODUCTION

As most granular materials are opaque for light in the visible spectrum, standard CCD cameras will only obtain information from the surface of a granular sample. But this surface behavior is known to differ substantially from the bulk properties.^{1–4} In contrast, X-rays will penetrate most granular samples with an intensity exponentially decaying with the length of the penetrated material, the so called Lambert-Beer law.^{5,6} Images obtained by placing a sample between an X-ray source and a camera with a scintillator are called radiograms. These have e.g. been used to study density variations in flowing sand^{7–10} or motion of larger objects inside a granular sample.^{11–14}

If these radiograms are collected while rotating the sample over a sufficiently large angle¹⁵, a number of mathematical algorithms can be used to reconstruct the sample in three-dimensions,¹⁶ a process called Computed Tomography. The volume data obtained this way consist of individual voxels, a linguistic blend of the words volume and pixel. Each voxel represents the x-ray absorption coefficient within a little cube at the corresponding location in the sample.¹⁷

Driven initially by medical research and then also material science, X-ray tomography has become a turnkey solution for three-dimensional imaging. In fact, it is now even possible to assemble your own custom-made X-ray tomography system.¹⁸ However, going beyond impressive images created with the 3D visualization software provided by the manufacturers does require serious image processing. The main objective of this article is to facilitate this step by providing a novice-friendly description how to identify the individual particles in a granular sample and then to compute both global statistical quantities and local quantitative measures.

The parameters discussed in this paper are however by far not the only properties that can be accessed from volume data. In the last decade X-ray tomography has been used to analyze the local structure of packings,^{19–29} understand their mechanical stability,^{30–32} and the forces at interparticle contacts.^{33–35} More dynamical properties studied include the formation of shear bands,^{36–41} the flow and compaction of rods,^{42–49} segregation,^{50,51} order-

disorder transitions,^{52–54} granular media as a model system for glassy behavior,^{55,56} and the crushing of individual sand grains.^{40,57}

The remaining article is structured as follows: Section II describes how to visualize and inspect the raw volume data. Section III provides the foundation for all subsequent analysis steps by describing how to identify the coordinates (and possibly orientations) of all the individual particles in the volume data. These coordinates will then be used to compute pair correlation functions (section IV), contact numbers (section V), and Voronoi volumes (section VI).

This paper is meant to be self-contained. It allows the reader to test all methods and reproduce all results by providing a) a demo volume data set of a sphere packing, which can be downloaded from⁵⁸, and b) the complete software package (as supplementary material and on github). The software should compile on any standard 64 Bit Linux PC, for convenience we provide also static linked binaries for all analysis step. The technical details how to obtain and run the analysis programs can be found in appendix A.

While most of the paper pertains to the analysis of a sphere packings, we will also comment on packings of ellipsoids and tetrahedra. Moreover, while this article was written with volume data obtained from X-ray tomography in mind, most of the described algorithms are rather generic and should work well with volume data and particle coordinates obtained from magnetic resonance imaging or laser sheet scanning in index matched samples.^{59–61}

II. VISUALIZING RAW DATA

Every commercial X-ray tomography setup will come with a software which not only allows you to reconstruct the volume data of your granular packing but also to visualize this volume in a number of ways. However, as this software is usually a closed-source program, it is a dead-end road for any advanced analysis of the data. Therefore the first step is to export the data as a three-dimensional volume file, which is typically accompanied

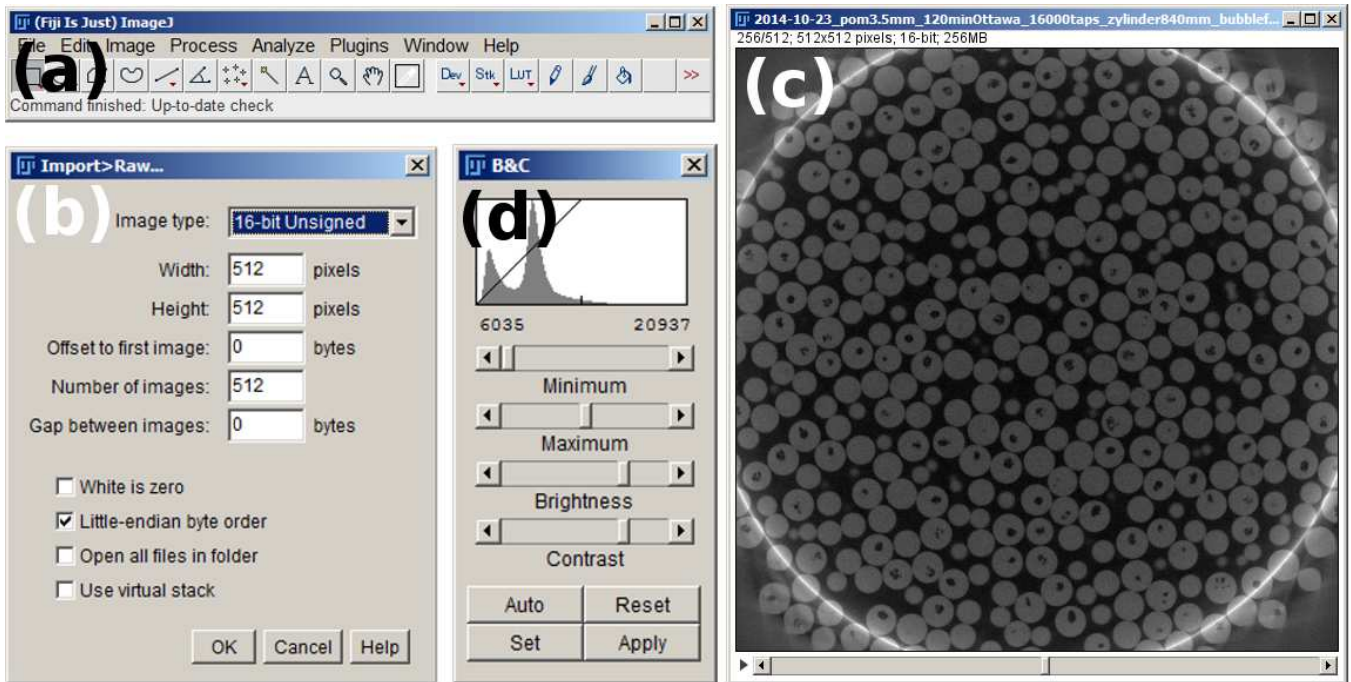


FIG. 1. Visualizing raw data in Fiji. (a) Fiji’s main window after starting the program. (b) import raw dialogue, here listing the parameters needed for visualizing the example data. (c) one XY slice of the example volume when imported to Fiji. (d) the brightness and contrast dialogue allows to adjust the look up table for displaying the image data.

by a small text file which contains the size information required to read this volume. If the manufacturer of a 3D imaging setup is not willing to provide such an export option this should be considered a deal-breaker.

After exporting the volume data set, you might want to inspect it visually and possibly also preprocess it. A powerful and open source software for these purposes is Fiji. Fiji is written in Java and uses multiple windows to perform its tasks; the main window which appears after startup is shown in figure 1(a). For more information on how to obtain and run Fiji, see appendix A 2.

To load the volume data, open the import RAW dialogue, shown in figure 1(b) by selecting *File* → *Import* → *RAW* from the menu bar. Here you will need to provide a number of parameters that can be divided in three groups: volume specific, visualization choices, and machine specific. The most important ones are the volume specific parameters, *Width*, *Height* and *Number of Images* which represent the dimensions of the volume in x , y , z respectively. To open the example dataset accompanying this paper, you will need to insert the values shown in figure 1(b). A detailed description of all parameters in the dialogue is given in appendix A 2.

After the import of the raw file is complete, a new window will open, which will show the central XY-slice of the volume. For the example data it should look like figure 1(c). The slider at the bottom of the window allows to scan through all slices of the volume. When moving the mouse over a voxel of the image, the respective coordinates within the image and the voxel’s grey value will be shown in the status bar in FIJI’s main window.

To evaluate individual features of an image, it is often necessary to adjust the brightness and contrast of the

image. This can be done by selecting *Image* → *Adjust* → *Brightness/Contrast* from the menu bar. The dialogue shown in figure 1(d) will open up, allowing you to tweak the respective values. The figure in the top part of the window shows the gray value histogram and the look up table (indicated by the straight line) used in the image window. The latter indicates how the gray value in the image will be mapped onto the gray values on the screen (represented by the vertical axis). This look up table can be adjusted either by changing the minimum and maximum sliders or the brightness and contrast sliders.

Often it is also beneficial to look at a different projection of the volume data. The default view after loading shows a XY slice through the volume. To change the projection plane, select *Image* → *Stacks* → *Reslice*. Leave all parameters on the default settings and click ok. This will create a XZ projection of the volume that will open in a new window.

III. FINDING PARTICLES

The first and most important step in analyzing the volume file is to detect the positions (and for non-spherical particles also orientations and size) of all individual particles in the sample. The resulting list of particle coordinates is the input data for all subsequent analysis steps. The difficulty of this image processing step comes from the inherent measurement noise and imperfections which create ambiguities how to assign individual voxels to specific particles.³⁴

For monoschematic particles, such as spheres, ellipsoids, cylinders or tetrahedra, this problem becomes

much simpler, because the a-priori knowledge of their shape can be used in particle detection and boundary detection between neighboring particles.

Only very recently, level-set method have been developed⁶²⁻⁶⁴ which allow to reliably identify the positions and orientations of non-monoschematic particles such as sand grains.

The choice of the image processing chain will in general depend on the shape of the particles, the quality and resolution of the raw data and the effort one is willing to take to optimize accuracy and detection rate. In this paper, we will describe a rather generic algorithm based on erosion and the Euclidian Distance Map.⁶⁵ This algorithm has been successfully used for identifying both spheres and ellipsoids.^{66,67} All steps of the image processing chain have been included into a single program, `volume2positionList`. Appendix A3 describes how to run it with the demo volume data set. Additionally, the C++ source code can be downloaded from⁶⁸ and serve as a starting point for code adapted to your specific problem (`volume2positionList` is published under the GPL v3 open source license). However, depending on your volume data, you might need to adapt the parameters of the program or even want to consider other image processing approaches, such as a direct watershed transformation^{26,32,34,35} or cross-correlation with template images.^{29,69}

This section is split into three parts. In section III A we describe the image pre-processing steps necessary to obtain a reliably binarized image where all voxels belonging to any of the particles are set to a grey value of one while the rest is set to zero. Some of these steps are necessary to compensate for deficiencies of x-ray tomography (noise, beam hardening), others are required due to imperfections of the particles. Then in section III B we describe how to assign all white voxels to the correct particle so that their center of mass positions can be computed. For spherical particles this is equivalent to the particle's center position. Finally, section III C discusses an image processing approach suitable for particles with flat faces such as cubes or tetrahedra.

A. Image Pre-processing

1. Radial intensity correction

Most X-Ray tomograms are taken with X-rays sources creating a broad spectrum of wave lengths; the only relevant exception are monochromatic beams at synchrotrons. As the absorption coefficient μ of all materials depends in a nonlinear way on the the wavelength of the X-rays, the assumption of an exponential decay of the X-ray intensity with thickness of the material is oversimplified.⁷⁰ A strictly exponential decay is however the basic assumption underlying most tomographic reconstruction algorithm; the resulting artifacts in the volume data are called beam hardening.

In our example beam hardening leads to a radial gradient in the grey value distribution with brighter voxels at larger radii and lower grey values at the center of the

sample. The effect becomes especially apparent by averaging the grey values in azimuthal rings (in cylindrical coordinates (r, θ, z) : average over z and θ) which is plotted in figure 2(a). This inhomogeneity has to be corrected before the binarization step which is based on a single threshold for the whole dataset.

Figure 2(b) shows a slice of the original tomogram on the left side and the radially corrected version on the right side. To obtain the homogeneous grey value distribution, the grey value of each voxel is divided by a correction factor which is determined from its radial position and an interpolation of the azimuthally averaged grey values shown in figure 2(a).

The radiograms taken during the acquisition of the the tomogram do not contain sufficient information to reconstruct the outmost parts of the tomogram correctly. In the left half of figure 2(b) this area corresponds to the bright circle and all parts even further away from the center. This area is set to black and thus removed from the further image processing and particle detection.

2. Bilateral Filter

An unavoidable consequence of the mathematical principles underlying the reconstruction of tomographic images from radiograms is that the signal to noise ratio decreases with increasing spatial frequency.¹⁶ This inherent noise is especially problematic if a voxel's grey value is close to the threshold of the binarization, which is the next step in the image processing pipeline. The noise can then lead to this voxel not being correctly identified.

A common remedy to reduce the noise is to low-pass filter the raw data with a Gaussian filter. This filter loops over all voxel positions \vec{x} in the volume file and computes:

$$f_{\text{gaussian}}(\vec{x}) = k \sum_{\vec{\eta}} o(\vec{\eta}) \cdot g(\vec{x} - \vec{\eta}) \quad (1)$$

where $f_{\text{gaussian}}(\vec{x})$ and $o(\vec{x})$ are the grey value of the filtered and the original image at position \vec{x} and k is a normalization factor. The sum runs over all voxel positions $\vec{\eta}$ in a predefined neighborhood of \vec{x} and g is a Gaussian function representing the geometric distance between the voxels at \vec{x} and $\vec{\eta}$. The mean of g is 0 and its standard deviation σ_g can be used to control the extent to which the grey values at $f_{\text{Gaussian}}(\vec{x})$ are blurred.

A significant downside of the Gaussian filter is that it does not take the absolute differences between grey values into account and is thus blurring the edges in the image. To avoid this effect we apply a bilateral filter⁷¹ which reduces experimental noise without blurring edges. It does so by multiplying the sum with a second Gaussian term $p(o(\vec{x}) - o(\vec{\eta}))$ (mean 0, standard deviation σ_p) which represents the photometric distance i.e. the grey value difference between the two voxels under consideration:

$$f_{\text{bilateral}}(\vec{x}) = k(\vec{x}) \sum_{\vec{\eta}} o(\vec{\eta}) \cdot g(\vec{x} - \vec{\eta}) \cdot p(o(\vec{x}) - o(\vec{\eta})) \quad (2)$$

Figure 2(c) shows an enlarged area of the tomogram before (left half) and after (right half) bilateral filtering.

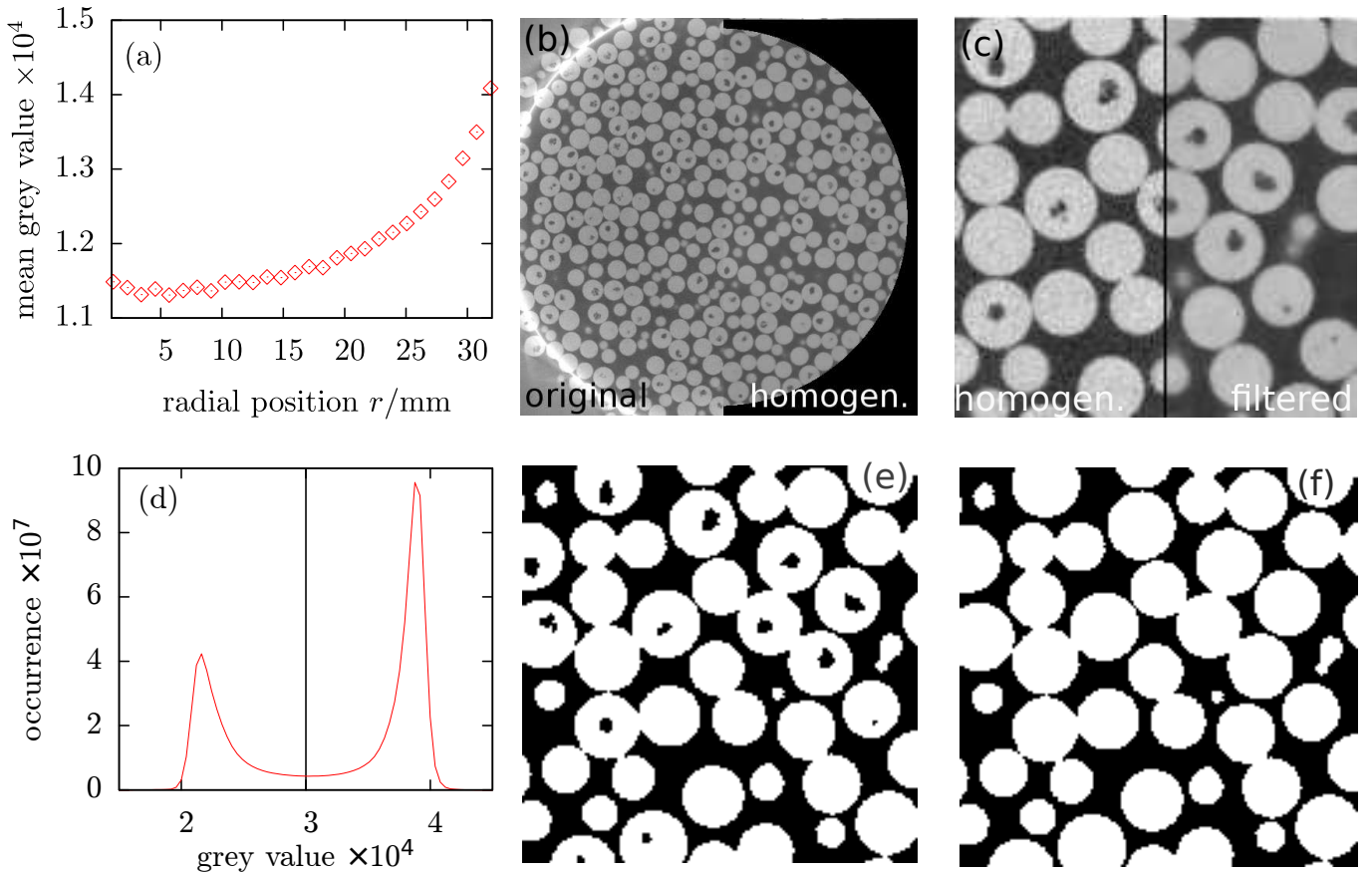


FIG. 2. Pre-processing steps of the example tomogram. (a) The azimuthally averaged grey values. Beam hardening leads to increasing grey values with distance from the center axis of the tomogram. (b) A tomographic slice. left half: original image data. Right half: after the radial intensity correction. The outer regions are set to black. (c) A small area of the homogenized (left half) and filtered (right half) volume. (d) The histogram of all grey values. The left peak correspond to air voxels, the right peak to particle voxels. The black line is the binarization threshold calculated by Otsu’s method. (e) A slice of the binarized volume, which shows voids inside the particles. (f) Same slice as in panel e but after filling the internal voids.

In general, the standard deviations of the two Gaussian functions, σ_g and σ_p , have to be adapted to the image material at hand. For the sample data, choose $\sigma_g = 1.75$ (in units of voxel sidelength) and $\sigma_p = 2000$ (in units of grey values).

3. Binarization

The next step in the image processing chain is to create a binary volume where all voxels belonging to particles are assigned a value of one (white) and all voxels representing air are assigned a value of zero (black). This assignment is solely determined by a grey value threshold. Figure 2(d) shows the grey value histogram of our pre-processed demo volume, the lower peak is formed by the air voxels, the higher peak represents voxels from particles. The optimal threshold, indicated by a vertical line in figure 2(d), is calculated using *Otsu’s* method:⁷² it minimizes the weighted sum of the standard deviations of the two populations created by this threshold. Figure 2(e) displays the same area as figure 2(c) but after binarization.

4. Filling internal voids

A frequent imperfection in commercially available granular particles are cavities created during the manufacturing process, especially but not exclusively during injection molding. In order to not obstruct the calculation of the centroid of each particle, these voids have to be removed. If the voids are completely internal, i.e. they are not connected to the exterior of the particle, they can easily be corrected by the following algorithm: Using the Hoshen Kopelman algorithm described in appendix B, all clusters of black voxels are identified. The largest of these clusters is the air surrounding all particles, all other clusters are cavities inside of particles. By setting the voxels of all but the largest clusters to 1, these cavities will be filled. The result of this operation is shown in figure 2(f).

In case the voids are connected to the outside of the particle, an improvement of the raw data can still be obtained by applying above algorithm to the individual slices in alternating orientations.⁶⁹

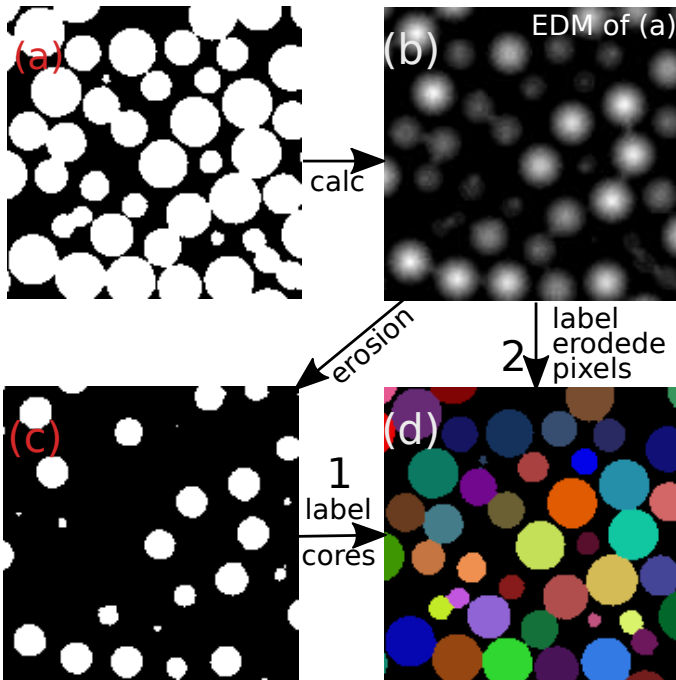


FIG. 3. Identifying particles by assigning the white voxels using the Euclidean Distance Map. (a) Slice of the binarized volume after the voids inside the particles have been filled. (b) Euclidean Distance Map (EDM). The voxel's grey value corresponds to its distance to the nearest black voxel. (c) the eroded volume, separating the particle cores. (d) the processed volume, different colors correspond to different particle IDs.

B. Identifying particles using the Euclidean Distance Map

Purpose of this step is to assign to each white voxel, i.e. voxel belonging to a particle, a number (the particle ID) that identifies to which particle this voxel belongs. Then the position of each particle can be computed as the centroid of all its voxels.

This is done by first computing the *Euclidean Distance Map* (EDM). In the EDM each white voxel is assigned the geometric distance (in units of voxels) to the closest black voxel. Thus all black (air) voxels are assigned 0. In consequence, the center voxels of the particles are assigned with the highest values, as they are farthest away from any black voxel. Figure 3(b) shows the EDM of the binarized image in figure 3(a).

The EDM is then the starting point of a two step algorithm. In a first step, the particles are separated using image erosion. The remaining separated particle cores are labeled. In a second step all voxels, which have been eroded in step one, are assigned to their respective particle cores.

After binarization all particles form, due to their contacts, one connected white blob. The erosion step separates this blob into individual particles by removing an outer layers of thickness λ . Practically, this is done by thresholding the EDM with the chosen erosion depth λ ; all voxels with an EDM value smaller than λ will be set to black, the remaining to white. Figure 3(c) show the

erosion result of our demo slice with $\lambda = 5$. Similar to the two σ values of the bilateral filter, the value of λ has to be adapted to the respective volume data. If λ is too small, it will not remove all the connections between individual particle clusters. If λ is too large, particles will be eroded completely away. Finally, the voxels in the now separated particle cores are assigned an unique label, the particle ID, using the Hoshen Kopelman algorithm described in appendix B (this time working with the white voxels).

In the second step all voxels, that have been eroded in the first step, have to be assigned their correct particle ID. This is achieved by performing an uphill gradient search on the EDM which will point for each voxel to the closest particle center. Figure 3(d) shows the labeled version of our demo slice with each color representing another label.

The labeled volume contains also clusters of particles that touch the radial cut that has been done during image pre-processing, as well as particles that touch the bottom and top of the volume. Those clusters have to be removed from the labeled volume, because they do not correspond to completely detected particles. This is done by removing all clusters from the labeled image, which are closer than one particle diameter to the radial boundary or that touch the bottom or the top slice of the tomogram. If the analysis boundary coincides with a smooth container boundary, strong layering effects will occur^{1,3,4} and the subsequent analysis should ignore rather three to four of the outmost layers.

The labeled image can now be used to calculate the centroid of each particle by averaging the coordinates of all voxels with the same label. The precision of the centroid will depend on the accuracy of the detection of the boundary voxels of the particle. However, due to the large number of boundary voxels, typically sub-voxel accuracy can be expected. A method to measure this accuracy will be discussed in section IV. Additionally, counting the number of voxels of each label will yield the volume of the respective particle. The list of particles centers, volumes and IDs is the main result of the image processing chain.

After removing the only partially detected particles at the boundaries, the volume distribution of the remaining particles should be rather narrow peaked, reflecting the narrow size distribution of the particles as well as the imaging system resolution. The presence of particles with roughly two or three times the average particle volume indicates that the erosion depth λ has been chosen to small.

The algorithm discussed in this section works well for monodisperse spheres and ellipsoids.^{66,67} For ellipsoids not only the center of mass, but also lengths and orientation of each ellipsoid's axis have to be determined. This can be done by computing the equivalent of the moment of inertia tensor (as described in section VI C) of all voxels belonging to an ellipsoid. In general, the algorithm described above can be expected to be suitable for all types of regular particles which are neither concave nor possess flat faces. A method handling particles, which can form face to face contacts, will be discussed in the next subsection.

C. Finding tetrahedra

Many granular materials such as salt or sugar are composed of constituents which are created by a crystallization process. The resulting flat faces of the particles quadruples the number of ways particles can form contacts (compared to the point-like contacts between spheres). This is demonstrated in Figure 4 for the example of two tetrahedra: there are face to face, edge to edge, and vertex to face contacts.

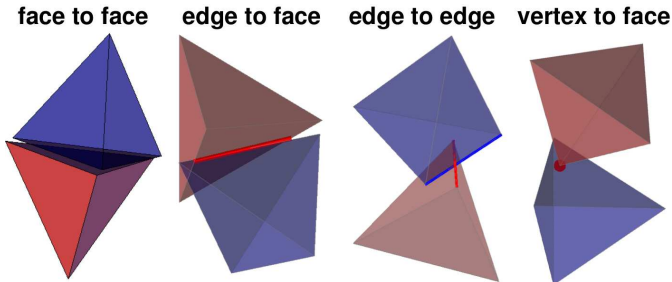


FIG. 4. The four different contact types found in tetrahedra packings.⁷³ Reproduced with permission from Phys. Rev. Lett. 111, 028001 (2013). Copyright 2013 APS.

The mechanical differences resulting from the different types of contacts will be discussed in section V. But the presence of face to face contacts is also a challenge for the development of particle detection algorithms because two tetrahedra forming a well aligned face to face have a joint minimum in the Euclidian Distance Map. Which implies that they can neither be separated by the erosion step described above nor a watershed transformation. Therefore an alternative approach to the particle detection problem is needed.

Figure 5 (a) and (b) depict a photograph of real tetrahedra as well as a rendering of the same tetrahedra after X-ray tomography and particle detection, thus demonstrating that the detection algorithm described in reference⁷³ works well for tetrahedra, resulting in detection rates larger than 99.8 %. The algorithm is based on a steepest ascend which is explained in figure 5 c: After preprocessing steps similar to the ones described in section III A, a tetrahedral probe body is translated, rotated and grown within the binarized sample in such a way that its overlap with voxels belonging to tetrahedral material is maximized. When the size of the probe body has reached the dimensions of an actual particle, a new tetrahedron has been found. After determining its center of mass and orientation, all voxels belonging to this tetrahedron will be set to black in order to facilitate the detection of the remaining particles. More details on the algorithm can be found in.⁷⁴

IV. PAIR CORRELATION FUNCTION

Typically, the first analysis step done after finding the particle coordinates is to compute the pair correlation function $g(r)$ (often also called radial distribution func-

tion). $g(r)$ describes how the average number density changes while moving away a distance r from an (arbitrary) reference particle. The two reasons for $g(r)$ being one of the first steps in most analysis is that it not only gives some insight in the structure of the packing but also provides a measure for the quality of the image acquisition and particle detection.

A discretized version of the pair correlation function can be computed by counting the number of particles in spherical shells around a reference particle:

$$g(r, \Delta r) = \frac{\langle N(r + \Delta r) - N(r) \rangle}{V_{\text{shell}} \rho} \quad (3)$$

$N(r)$ is the number of particles within a sphere of radius r around a given particle. $N(r + \Delta r) - N(r)$ corresponds to the number of particles in a spherical shell of radius r and thickness Δr (we assume here Δr to be small compared to r). The average $\langle \dots \rangle$ runs over all particles in the sample. In practise, the numerator is computed by calculating the center to center distance of all pairs of particles and then storing this information in a histogram.

The normalisation in the denominator consists of two parts. First the volume of the spherical shell V_{shell} does depend on r : $V_{\text{shell}} = 4\pi r^2 \Delta r$. Secondly, by dividing with the number density $\rho = \frac{N_{\text{tot}}}{V_{\text{tot}}}$ we assure that an uncorrelated system will have $g(r) = 1$.

In analyzing experimental data, Δr has to be chosen small enough to not smear out important features, but large enough to have good statistics in each bin. For the sample data $\Delta r = 0.005$ voxel works well. Another effect to be taken into account is the finite size of all experimental samples. The larger r becomes, the larger will be the number of particles for which at least a part of the spherical shell will be outside the sample volume and therefore empty. Consequentially, the experimentally determined $g(r)$ decays to zero for large distances r .

In an ideal gas, or any other system without correlations, $g(r)$ is a constant and set to one by the normalization with the average density. In an amorphous packing of monodisperse spheres, $g(r)$ will appear as in the inset of figure 6b. For distances shorter than a particle diameter d the value of $g(r)$ is zero, because the spheres cannot overlap. Finite values in this range point to either the presence of additional smaller particles or problems during image processing. At the distance of one particle diameter there is a strong peak, which is formed by all the pairs of particles which are in contact. Due to both the polydispersity of the particles and noise in the experimental data, this peaks will be broadened. This effect which can e.g. be seen in the main plot in figure 6 (b) will be discussed in more detail below. In amorphous systems without far-reaching order there are other small peaks of $g(r)$ for the values of $\sqrt{2}d$, $2d$, and $\sqrt{3}d$, which is shown in the inset of 6 (b). But for larger distances $g(r)$ approaches the value of one characteristic for disordered systems (aside from the finite size effects discussed above).

$g(r)$ does provide important insight into structural differences between packings of spheres^{19,21,22,75} rods,⁴⁶ ellipsoids,⁷⁶ tetrahedra,⁷³ or granular chains.⁷⁷ Figure 6c demonstrates for example that in packings of tetrahedra

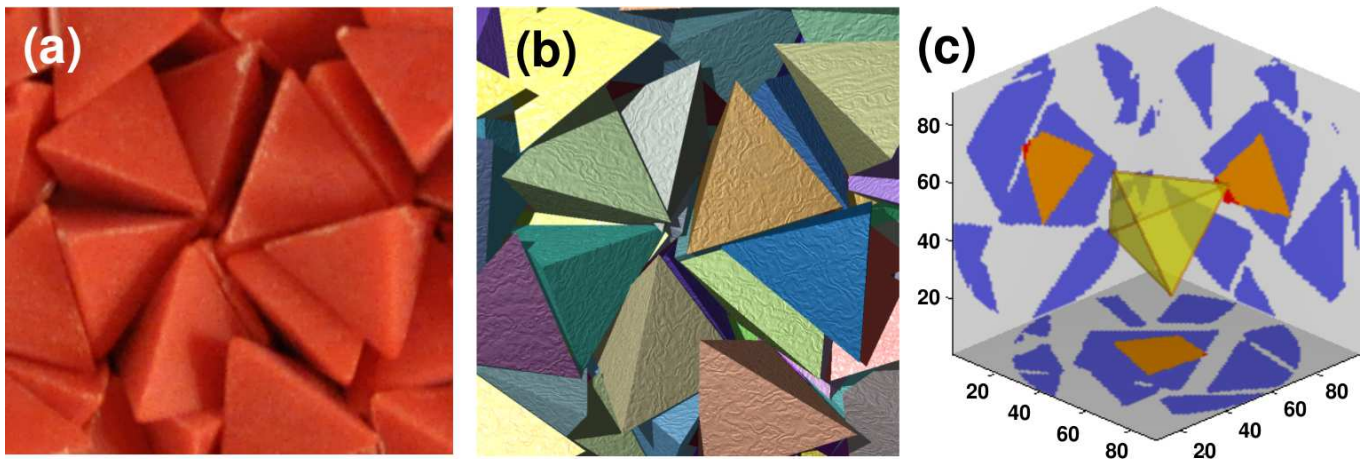


FIG. 5. Detecting tetrahedra. (a) Photograph of packing surface. The tetrahedra are made of polypropylene and have a side length of 7mm. (b) Rendering of the particles detected in the same sample. (c) Visualizing the steepest ascend algorithm. The three sidewalls of the cube are orthogonal cuts through the volume with gray corresponding to the empty space between the (blue) particles. The yellow tetrahedron in the center represents the probe body which is translated, rotated, and grown in order to maximize the overlap (indicated by orange) with voxels belonging to particles and minimize the overlap with air voxels (shown in red).⁷³ Reproduced with permission from Phys. Rev. Lett. 111, 028001 (2013). Copyright 2013 APS.

the closest possible distance is *not* the most likely contact configuration.⁷³ This effect is a consequence of the lower probability of a perfect face-to-face alignment compared to either slightly shifted face-to-face or low angle face-to-edge contacts. Within the jamming paradigm,^{78,79} the shape of the first peak of $g(r)$ is used to derive how the number of contacts in a packing of compressible spheres will change with pressure. Figure 6c asserts that these scaling laws will not be applicable to packings of soft tetrahedra.

In an ideal world of absolutely monodisperse, hard spheres and zero error in the coordinate detection, the left shoulder of the first peak of the pair correlation function would be a step function. The shape of the right shoulder will reflect the extent to which particles have almost formed contacts. For frictional particles the exact analytic form of this decay is not known, but the results discussed below indicate that it will also be a steep decay. In praxis any broadening of the first peak can therefore be traced back to the polydispersity of the spheres and/or experimental noise.⁸⁰ The latter is usually well modeled by a Gaussian distribution, the former can often be approximated by a Gaussian.

Figure 6a shows a Gaussian fit to the first peak in the $g(r)$ of our demo dataset. The two fit parameters are the mean of 27.177 voxels and the standard deviation σ of 0.036 voxels. The mean value corresponds to the interpolated maximum of $g(r)$, which is the most frequent separation two sphere centers will have. It is therefore our best estimate for the mean diameter of the spheres d_{mean} . The quality of this method to determine average particle diameters is demonstrated in a study of segregation in a polydisperse system⁵⁰ where d_{mean} changes of fractions of a percent can be detected reliably.

The standard deviation σ of the Gaussian fit is a convolution of the effects of polydispersity, experimental noise and particle detection. If the experimental data are taken

with sufficiently monodisperse spheres, σ can be used to characterize the quality of the image acquisition (figure 6 (b), taken from,²⁹) compare the quality of different sphere detection algorithms (figure 6 (d), taken from⁶⁹), or even compare different imaging methods (X-ray versus neutron tomography⁸¹).

Pair correlation functions for the example data can be calculated with **raps**,⁸² which can compute also a number of other structural characteristics of sphere packings. **raps** is licensed under the LGPL and is free to use, further details can be found in appendix A 4. The fit to the first maximum of $g(r)$ shown in figure 6 (a) can be performed with a script described in appendix A 5.

V. DETERMINING CONTACT NUMBERS

For a granular packing to be mechanically stable, its particles need to have enough contacts Z to block all their translational and rotational degrees of freedom. The minimum number of contacts necessary to achieve this is the so called isostatic contact number Z_{iso} . For frictional spheres⁷⁸ Z_{iso} equals four. Determining Z has always been a desired experimental goal. Before the advent of tomographic imaging, researchers had mixed particles with small amounts of paint which was then attracted to the contact points by capillary forces. After the paint had dried, the packing could be disassembled and the analysis of the paint marks at the surface allowed to estimate Z for packings of spheres^{83,84} and cylinders.⁸⁵

The availability of tomographic images seems to allow the direct observation of contacts in form of connected pathways of voxels between particle centers. However, in practice this idea is hard to realize.^{34,35} The actual contact between hard particles is formed in a small area only, corresponding to a small number of voxels. Even a minor error in the choice of the binarization threshold

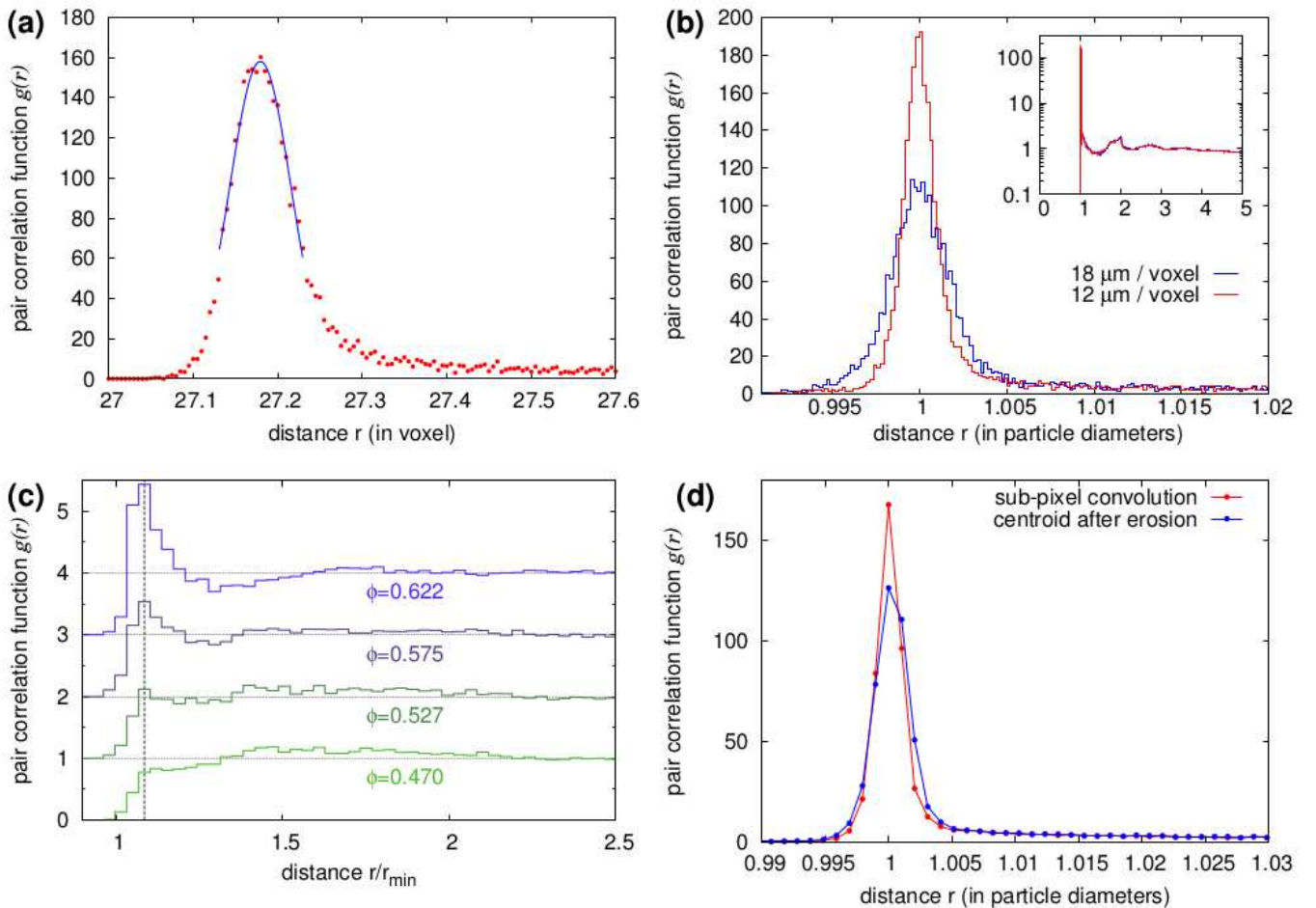


FIG. 6. Information provided by the first peak of the pair correlation function. (a) A fit of the first peak of the pair correlation function with a Gaussian (blue line) provides a precise estimate of the average diameter of the spheres. Data points are from the analysis of the demo data set accompanying this paper. (b) The influence of the spatial resolution of the tomograms can be demonstrated with packings of highly monodisperse spheres ($d = 351 \pm 0.5 \mu\text{m}$). Figure reproduced with permission from Soft Matter 12, 3991 (2016). Copyright 2016 Royal Society of Chemistry. (c) For tetrahedra the shortest possible distance r_{\min} , which is approximately 0.408 times the side-length, is not the most likely distance between individual particles (indicated by a vertical dashed line). Offsets have been added for improved visibility. Reproduced with permission from Phys. Rev. Lett. 111, 028001 (2013). Copyright 2013 APS. (d) Datasets of sufficiently monodisperse beads ($d = 351 \pm 0.5 \mu\text{m}$) do also allow a comparison of different particle detection algorithm.⁶⁹

can erase or fill erroneous voxels and therefore make the detection going completely wrong.

An alternative approach is to a) not consider contacts between individual particles but to compute Z from the whole ensemble of particles at once using their center of mass coordinates. And b) to rely on the information contained in the whole surface of the particles, not only at the position of potential contacts. The second point is already used in our particle finding algorithm: small mistakes in the binarization threshold will influence all voxels at the particle boundary the same way. The resulting over-erosion or dilation is radially symmetric and will therefore have only a small influence on the determined center of mass.

Point a) is exploited by using the information from the ensemble of all particles to first determine the best estimate for the particle diameter itself (as discussed in section IV) and then to fit a model to the data which allows

to identify both Z and the strength of experimental noise and polydispersity. This ensemble based fitting method is described in more detail in the next subsection. The basic idea for this approach has first been suggested and applied by.^{21,22} In the last years the method has then been used to determine Z for packings of spheres and ellipsoids,^{65,66} tetrahedra,⁷³ and cylinders.⁸⁶

A. Ensemble based fitting

This approach to determine the global contact number Z works on the basis of the information contained in the first peak of $g(r)$. The first step is to endow all particle centers in the packing with a virtual diameter x and then determine the average contact number $I(x)$ of this packing by counting the number of intersections between these virtual spheres. For monodisperse spheres, $I(x)$ is

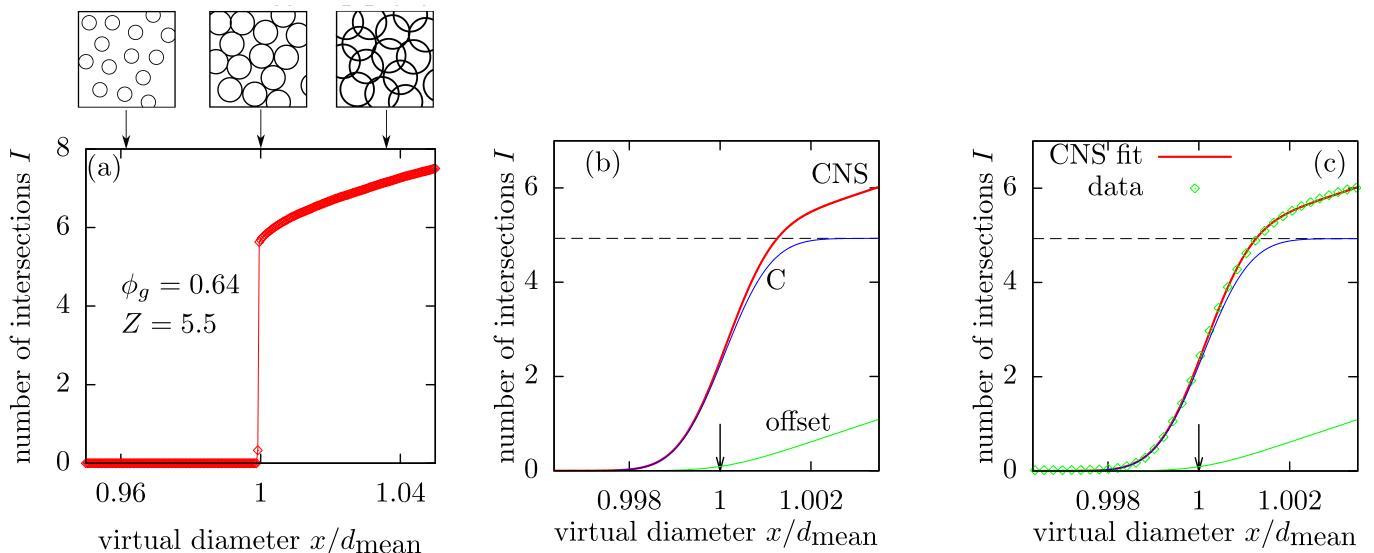


FIG. 7. Determining Contact numbers by fitting the Contact Number Scaling function to the experimental data. (a) The number of intersections between spheres $I(x)$ in an ideal (monodisperse, noise free) world. The three images at the top show two-dimensional schematics for different virtual side lengths x . (b) The CNS function and its components. (c) A fit of the CNS function to experimental data.

equal to an integral over $g(r)$ up to the value x .

Figure 7(a) depicts $I(x)$ for an idealized dataset of monodisperse spheres and in the absence of experimental noise. As the data in figure 7(a) has been extracted from a packing created by simulation,⁸⁷ these conditions are indeed fulfilled. For $x < d_{\text{mean}}$ there are no intersections at all, thus $I(x)$ is zero. At the actual sphere diameter d_{mean} , I jumps to the global contact number Z . And for larger values of x , I keeps increasing due to the formation of spurious contacts. Modeling this behavior results in a function $Z \cdot \theta(x - d_{\text{mean}}) + \text{off}^{\text{ideal}}(x)$ with θ being the Heaviside step function and of $\text{off}^{\text{ideal}}(x)$ modeling the a priori unknown increase of Z above d_{mean} .

In any experimental system, the particles are not ideally monodisperse and there will be experimental noise in the imaging system. These effects are similar to convoluting the above described ideal model with a Gaussian function. The resulting model is called Contact Number Scaling (CNS) function:

$$\begin{aligned} \text{CNS}(x) &= C(x) + \text{off}^{\text{real}}(x) \\ C(x) &= Z/2 \cdot (\text{erf}(\sigma \cdot (x - d_{\text{mean}})) + 1) \end{aligned} \quad (4)$$

with σ being the width of the error function. Examples of $\text{CNS}(x)$, $C(x)$, and $\text{off}^{\text{real}}(x)$ are shown in figure 7(b).

By fitting equation 4 to the experimental $I(x)$ as shown in figure 7(c), the global contact number Z can be determined. Here d_{mean} is not a fit parameter as it has already been determined from the Gaussian fit to $g(r)$ discussed in section IV. If Z is determined for a larger series of tomographies all taken with identical imaging conditions, the number of effective fit parameters can be reduced further as neither the polydispersity nor the experimental noise will depend on the individual experiment. Consequently, σ should also be the same for all experiments. We can therefore perform a second round of fits where σ

is held constant at a value which is the mean of the first round of fits.⁷³

$I(x)$ can be computed using `raps`. It is then stored in a file named `cns_example.dat`. A detailed description of the fit procedure can be found in appendix A 5; a minimal fit script based on the open source program `gnuplot`⁸⁸ is part of the supplemental material.

Once the global contact number Z has been measured, we can also identify a local contact number Z_l as the overlap between individual particles after their size has been rescaled such that the average of Z_l is identical to Z . Especially for frictional particles, Z_l shows a strong dependence on the local volume fraction^{66,89} which will be introduced in section VI A. For particles with different types of contacts, such as tetrahedra, a further step of image processing is required to determine the type of contact from the angle between the surface normals of the involved faces.⁷³ Finally, a number of other measures, such as e.g. fabric anisotropy,⁹⁰ require knowledge about the position of the individual contacts between particles.

VI. VORONOI VOLUMES

Any attempt to understand granular physics based on the behavior of its individual constituents will need to provide a definition of what is considered the local environment of a particle.^{27,91–95} For monodisperse spheres the by far most common definition is provided by the Voronoi tessellation: the space in the sample is divided into cells such that each cell contains all points that are closer to the center of a given particle than to any other particle center. Figure 8(a) illustrates this idea using a two-dimensional packing of monodisperse discs, figure 9(a) shows the Voronoi cells of a sphere packing. Unlike some of the competing partitioning schemes,⁹⁶ it

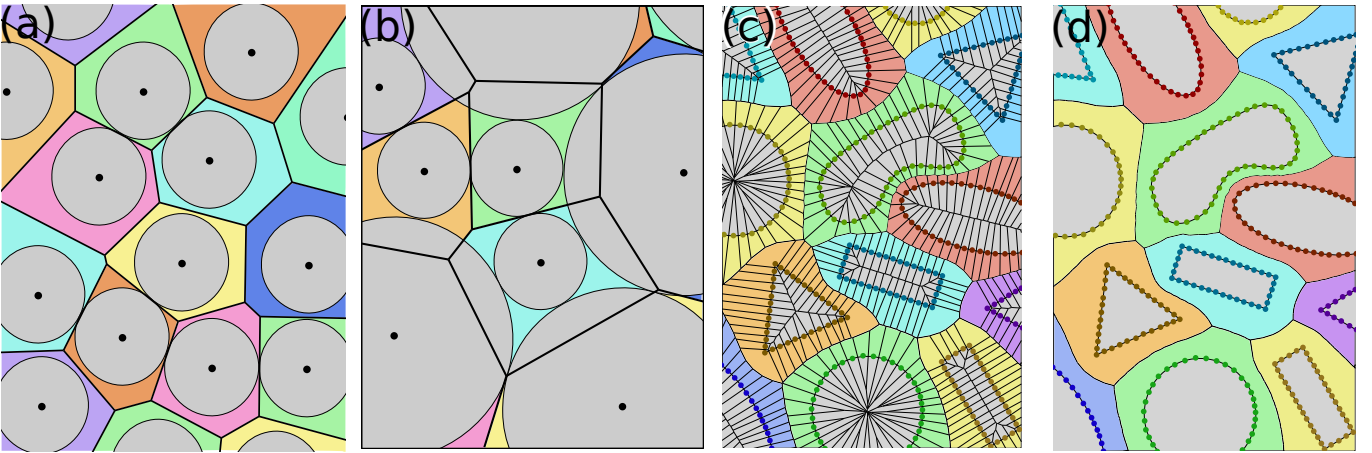


FIG. 8. Two-dimensional Voronoi and Set Voronoi diagrams. (a) A Voronoi tessellation of monodisperse discs. (b) Voronoi diagrams are not well suited for a system of polydisperse discs. (c) The first two steps of calculating a Set Voronoi Diagram. First points are spawned on the surface of the particles. Then the classical Voronoi diagram for those points is calculated. (d) The Set Voronoi cells are calculated by merging all Voronoi cells that belong to the same particle.

is well defined in both two and three dimensions and it is space-conserving. The latter allows us to define a local volume fraction ϕ_l .

Voronoi diagrams have a number of geometrically and physically interesting properties. For example, the Voronoi volume distribution of sphere packings is well described by Gamma-distributions^{23,97-99} and independent from the experimental or numerical protocol the packing was created with. This result has also been generalized to cuboidal granular media.¹⁰⁰

A. Local volume fraction

The local volume fraction assigns each individual particle a local density. It is defined as

$$\phi_l = \frac{V_p}{V_c} \quad (5)$$

with V_p the volume of the particle and V_c the volume of its cell.

Local volume fractions provide a convenient way to compute the global packing fraction ϕ_g from a subset of all particles, thereby e.g. avoiding systematic errors in the ϕ_g values due to ordered layers and inaccessible space at container boundaries.^{3,4} However, while volumes are additive, volume fractions are not. Therefore the harmonic mean has to be used to calculate ϕ_g from the local packing fractions of the individual cells ϕ_l^i :

$$\phi_g = \frac{NV_p}{\sum_i V_c^i} = \frac{N}{\sum_i \frac{V_c^i}{V_p}} = \frac{N}{\sum_i \frac{1}{\phi_l^i}} \quad (6)$$

with V_c^i being the volume of the i th Voronoi cell and N the total number of particles.

Figure 9(b) demonstrates an interesting property of the local volume fraction distribution. Rescaling it with:

$$\phi_l^i = \frac{\phi_l - \phi_g}{\sigma(\phi_l)}, \quad (7)$$

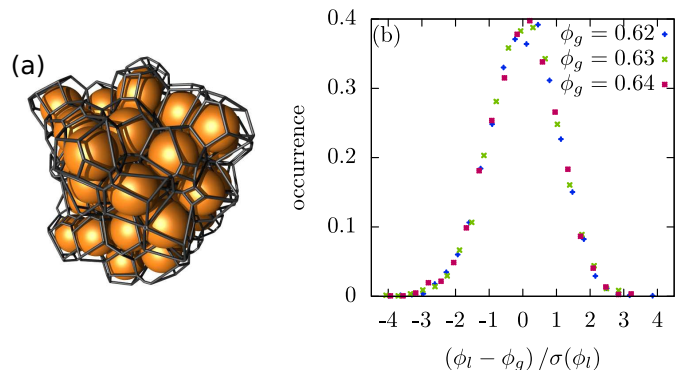


FIG. 9. Voronoi tessellation in three dimensions. (a) A subset of a packing of spheres with its Voronoi cells. (b) Rescaled distribution of local packing fractions from systems of monodisperse spheres at different global packing fractions ϕ_g .

where $\sigma(\phi_l)$ is the standard deviation of the distribution, results in a data collapse for packings taken at different values of ϕ_g . Even more unexpected is that this universality extends also to packings of oblate ellipsoids.^{66,67} Additionally, it can be shown that contact numbers in packings of spheres and ellipsoids are best explained by a theory starting from ϕ_l .⁶⁶

The local volume fractions of our demo data set can be computed using the program `pome1o`. Shape analysis of the Voronoi cells can be performed with the program `karambola`. Both programs will be introduced in the remainder of this section.

B. Set Voronoi tessellation

The normal Voronoi tessellation described above is not reliable for packings made from anything else than monodisperse spheres or disks. The underlying problem

is that a single point, the center of mass, is not sufficient to describe the spatial extension of the particle. Figure 8b demonstrates this for a packing of bidisperse disks: the volume of some disks does not belong to the Voronoi cell of that disk.

This problem is avoided by a generalization of the Voronoi tessellation, the *Set Voronoi* diagram (also called navigation map or tessellation by zone of influence).^{101,102} The Set Voronoi diagram uses the surface of the particles to assign the free space in between the particles. Thus each Set Voronoi cell contains the volume that is closer to the surface of its central particle than to any other particle surface.

Set Voronoi diagrams are usually numerically approximated. First the surface of the particles is discretized by spawning a grid of points on it. Then the packing is tessellated by calculating the classical Voronoi diagram for all surface points. These two steps are illustrated in figure 8c for a two-dimensional system of arbitrarily shaped particles. The final Set Voronoi diagram is then obtained by merging all Voronoi cells that belong to the same particle as shown in figure 8(d).

As discussed in section IV, experimental noise will lead to inaccuracies in the detected particle coordinates which will result in small overlaps between the particles surfaces. As this would lead to erroneous results during the calculation of the Set Voronoi diagram, all particles have to be shrunk sufficiently in size to resolve those overlaps. This step will influence for most particles the result of the tessellation; the amount of shrinkage should therefore be kept to a minimum.

1. Computing Set Voronoi diagrams

You can use the program `pome1o`¹⁰³ to calculate both Voronoi and Set Voronoi Diagrams. `pome1o` offers built-in functionality for common particle shapes, such as mono- and polydisperse spheres, ellipsoids, tetrahedra, and spherocylinders. Additionally, it offers a generic mode which allows to handle almost any particle shape. The command required to run `pome1o` on the example data is explained in appendix A 6.

While `pome1o` does compute the Set Voronoi cells and their volume, it does not characterize their shape geometrically. This task is handled by the program `karambola` discussed in the next subsection. Furthermore, in order to limit the size of the Voronoi cells of the outmost layers of particles detected, `pome1o` assumes that the sample is embedded in a rectangular box. This leads to erroneous large Voronoi cell volumes in these outer layers of the sample which have then to be discarded.

C. Describing Voronoi cells with Minkowski Tensors

The best way to quantify the shape and morphological properties of the (Set-) Voronoi cells is by computing their *Minkowski Tensors*.^{104,105} The importance of the Minkowski tensors is underscored by Alesker's theorem, which states any additive, motion-covariant, and contin-

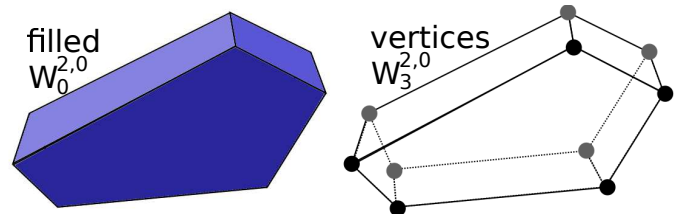


FIG. 10. Visualization of two of the six Minkowski tensors.

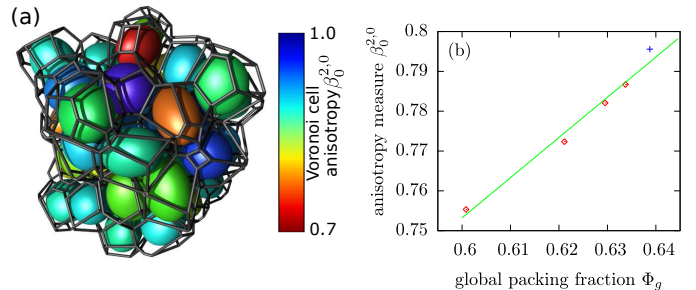


FIG. 11. Quantifying the shape anisotropy of Voronoi cells. (a) The same subset of the Voronoi diagram shown in figure 9a. The beads have been replaced by ellipsoids that match the anisotropy of the Voronoi cells. The anisotropy is quantified by $\beta_0^{2,0}$ and is also indicated by the color of the ellipsoids. (b) Average anisotropy measure $\beta_0^{2,0}$ as a function of the global packing fraction ϕ_g for systems of monodisperse spheres. The example tomogram that is provided with this document is marked as a blue cross.

uous function can be described by a linear combination of these six different tensors.¹⁰⁶

We will now examine two examples of Minkowski tensors closer. We start with a Voronoi cell as shown on the left side of figure 10. It can be described as a convex body K in Euclidean 3D space with a bounding surface S . The Minkowski Tensor $W_0^{2,0}$ is defined as:

$$\mathbf{W}_0^{2,0} = \int_K \vec{r}^2 dV \quad (8)$$

where \vec{r} is a position vector and the integral is over the volume of the filled cell. $W_0^{2,0}$ can therefore be compared to the moment of inertia tensor.

The right side of figure 10 illustrates $W_3^{2,0}$, which is defined as:

$$\mathbf{W}_3^{2,0} = \int_S \vec{r}^2 G(\vec{r}) dA \quad (9)$$

$G(\vec{r})$ is the Gaussian curvature of the surface, which is only non-zero on the vertices of the Voronoi cell. $W_3^{2,0}$ is akin a moment of inertia tensor where only the vertices of the Voronoi cell contribute.

Once the Minkowski tensors have been computed for a Voronoi cell, its shape anisotropy can be quantified as the ratio $\beta_V^{r,s}$ between the smallest to the largest eigenvalue of the tensor $W_V^{r,s}$. Thus, a cell with $\beta_V^{r,s} = 1$ is isotropic while smaller values indicate larger anisotropies.

Figure 11a shows the same Voronoi diagram as figure 9a but the spheres have been replaced by ellipsoids

with an aspect ratio identical to the $\beta_0^{2,0}$ values of the Voronoi cells. Figure 11b demonstrates that for packings of monodisperse spheres the mean eigenvalue ratio $\beta_0^{2,0}$ increases linearly ϕ_g . For crystalline packings $\beta_0^{2,0}$ reaches unity (corresponding to isotropic Voronoi cells). In the opposite limit of an equilibrium fluid with vanishing density, $\beta_0^{2,0}$ approaches the value 0.37, which is characteristic for Poisson point processes.¹⁰⁷ It has also been shown that the anisotropy of the Voronoi cells is independent of preparation or gravity.^{104,108}

1. Computing Minkowski tensors

The eigenvalues of the Minkowski tensors can be calculated using the program `karambola`^{105,109,110} using the files written by `pomelo` as input. Details can be found in appendix A 7.

`karambola` will also write a file containing the scalar Minkowski value $W_0^{0,0}$ which corresponds to the volume of the Voronoi cell (in units of voxels³). The average sphere diameter has already been determined from the radial distribution function in section IV, allowing us to compute a precise particle volume, again in units of voxels³. Thus the output of `karambola` can also be used to calculate the local packing fraction of all particles using equation 5.

VII. OUTLOOK

Real world granular materials rarely consist of monodisperse spheres. Their particles are sometimes concave, almost always polydisperse, and often only approximately monoschematic; coffee beans are a good example of this combination. There are two technological developments that will help granular physics to close this gap: 3D printing and advances in image processing.

3D printing has been around for a couple of decades in academic and industrial settings. But in the last years a number of innovative startups have entered the market and considerably lowered the price tag on these machines. One way of moving away from monodisperse spheres is to print particles with complex or even concave shapes (such as jacks or dolosse) and of varying size.^{111,112} The precision of the 3D printing process will then allow to still make use of the knowledge of their shape during image processing.

Alternatively, we can directly use natural materials such as sand and improve our 3D image processing to obtain trustworthy segmentation results. The development of level-set methods in the group Gioacchino Viggiani marks an important step in this direction.^{62–64} There exist also hitherto unrealized synergies with the community studying multiphase flow in porous media. In their x-ray tomography images of fluid distributions in porous media they are confronted with very similar segmentation problems.^{113–115}

Taking a step back we note that the spread of X-ray tomography in granular physics is part of a larger shift in physics and science in general. Modern measurement de-

vices allow the acquisition of larger and larger data sets. Which in turn enables us to test ever complexer hypothesis. However, the amount of data processing and reduction necessary to do so increases almost at the same rate as the amount of data. This article is a good example. Starting from a 300 MByte large volume file, we identify the roughly 150 kByte large list of coordinates to end up finally with several tens of Bytes telling us the volume fraction, contact number, and Voronoi cell anisotropy of the sample.

This massive increase of the importance of data processing challenges the historically grown model of scientific publishing because it strongly increases the danger of propagating undetectable errors made during this data processing step. Such errors might be innocent mistakes made by faithful scientists. Or they could be intentional cherry-picking to increase the impact factor of the result.

We believe that we need to change our understanding how scientific publishing as a process works: Raw data *and* the software needed to process them have to become an integral part of any scientific publications. There is already an established infrastructure for publishing the raw data in the form of open data repositories such as `Dryad`¹¹⁶ and `Zenodo`¹¹⁷. To open up the analysis, it is a good first step to publish the source code under an open source license such as the GPL. However, we will also need new tools and protocols that facilitate to document and preserve the individual choices (e.g. parameter values for image processing) made during the analysis. But these are technological, solvable problems. Getting the scientific culture to open up to this level of sharing will likely be more difficult, but at the same time it seems unavoidable. The intrinsic strength of this vision is best captured in a recent comment by Tal Yarkoni:¹¹⁸ I hope in 20 years we'll be amazed that scientists once blindly trusted results they couldn't press the "run" button on.

VIII. SUPPLEMENTARY MATERIAL

The supplementary material consists of source code, data and binaries and will be discussed in detail in the appendix A.

ACKNOWLEDGMENTS

We would like to thank Philipp Schönhöfer, Manuel Baur, Max Neudecker, Fabian Schaller, Gerd Schröder-Turk, and Song-Chuan Zhao for helpful discussions. This article started as a talk given at the Spring School "Imaging Particles" held in Erlangen, Germany in April 2016 and funded by German Science Foundation (DFG) through the Cluster of Excellence "Engineering of Advanced Materials" EXC-315. The development of the software described in this article was funded by the German Research Foundation (DFG) Forschergruppe FOR1548 "Geometry and Physics of Spatial Random Systems" (GPSRS). Figure 6 (a) has been reproduced from Ref.²⁹ with permission from the Royal Society of Chemistry.

- ¹W. Zhang, K. E. Thompson, A. H. Reed, and L. Beenken, "Relationship between packing structure and porosity in fixed beds of equilateral cylindrical particles," *Chemical Engineering Science* **61**, 8060–8074 (2006).
- ²A. V. Orpe and A. Kudrolli, "Velocity Correlations in Dense Granular Flows Observed with Internal Imaging," *Physical Review Letters* **98**, 238001 (2007).
- ³M. Jerkins, M. Schröter, H. L. Swinney, T. J. Senden, M. Saadatfar, and T. Aste, "Onset of mechanical stability in random packings of frictional spheres," *Phys. Rev. Lett.* **101**, 018301 (2008).
- ⁴K. W. Desmond and E. R. Weeks, "Random close packing of disks and spheres in confined geometries," *Physical Review E* **80**, 051305 (2009).
- ⁵J. H. Lambert, *Photometria, sive de Mensura et Gradibus Luminis, Colorum et Umbræ* (Eberhard Klett, Augsburg, 1760) <https://books.google.de/books?id=JdkTAAAAQAAJ>.
- ⁶Beer, "Bestimmung der Absorption des rothen Lichts in farbigen Flüssigkeiten," *Annalen der Physik* **162**, 78–88 (1852).
- ⁷R. L. Michalowski, "Flow of granular material through a plane hopper," *Powder Technology* **39**, 29–40 (1984).
- ⁸G. W. Baxter, R. P. Behringer, T. Fagert, and G. A. Johnson, "Pattern formation in flowing sand," *Physical Review Letters* **62**, 2825–2828 (1989).
- ⁹A. Kabla, G. Debrégeas, J.-M. d. Meglio, and T. J. Senden, "X-ray observation of micro-failures in granular piles approaching an avalanche," *Europhysics Letters* **71**, 932–937 (2005).
- ¹⁰A. J. Kabla and T. J. Senden, "Dilatancy in Slow Granular Flows," *Physical Review Letters* **102**, 228301 (2009).
- ¹¹J. R. Royer, E. I. Corwin, A. Flior, M.-L. Cordero, M. L. Rivers, P. J. Eng, and H. M. Jaeger, "Formation of granular jets observed by high-speed X-ray radiography," *Nature Physics* **1**, 164–167 (2005).
- ¹²R. D. Maladen, Y. Ding, C. Li, and D. I. Goldman, "Undulatory Swimming in Sand: Subsurface Locomotion of the Sandfish Lizard," *Science* **325**, 314–318 (2009).
- ¹³Y. Cao, X. Zhang, B. Kou, X. Li, X. Xiao, K. Fezzaa, and Y. Wang, "A dynamic synchrotron X-ray imaging study of effective temperature in a vibrated granular medium," *Soft Matter* **10**, 5398–5404 (2014).
- ¹⁴T. Homan, R. Mudde, D. Lohse, and D. van der Meer, "High-speed X-ray imaging of a ball impacting on loose sand," *Journal of Fluid Mechanics* **777**, 690–706 (2015).
- ¹⁵180° for a parallel X-ray beam, as e.g. delivered by a synchrotron. 360° if the beam expands from a point source, as in a normal X-ray tube.
- ¹⁶T. M. Buzug, *Computed Tomography - From Photon Statistics to Modern Cone-Beam CT* (Springer, 2008).
- ¹⁷The term voxel is used in two ways: to refer to the cuboidal image element itself and as a unit of length equivalent to one edge of this cube.
- ¹⁸A. G. Athanassiadis, P. J. L. Rivière, E. Sidky, C. Pelizzari, X. Pan, and H. M. Jaeger, "X-ray tomography system to investigate granular materials during mechanical loading," *Review of Scientific Instruments* **85**, 083708 (2014).
- ¹⁹G. T. Seidler, G. Martinez, L. H. Seeley, K. H. Kim, E. A. Behne, S. Zaranek, B. D. Chapman, S. M. Heald, and D. L. Brewae, "Granule-by-granule reconstruction of a sandpile from x-ray microtomography data," *Physical Review E* **62**, 8175–8181 (2000).
- ²⁰P. Richard, P. Philippe, F. Barbe, S. Boursès, X. Thibault, and D. Bideau, "Analysis by x-ray microtomography of a granular packing undergoing compaction," *Physical Review E* **68**, 020301 (2003).
- ²¹T. Aste, "Variations around disordered close packing," *Journal of Physics: Condensed Matter* **17**, S2361 (2005).
- ²²T. Aste, M. Saadatfar, and T. J. Senden, "Geometrical structure of disordered sphere packings," *Physical Review E* **71**, 061302 (2005).
- ²³T. Aste, T. D. Matteo, M. Saadatfar, T. J. Senden, M. Schröter, and H. L. Swinney, "An invariant distribution in static granular media," *Europhys. Lett.* **79**, 24003 (2007).
- ²⁴M. Tsukahara, S. Mitrovic, V. Gajdosik, G. Margaritondo, L. Pournin, M. Ramaioli, D. Sage, Y. Hwu, M. Unser, and T. M. Liebling, "Coupled tomography and distinct-element-method approach to exploring the granular media microstructure in a jamming hourglass," *Physical Review E* **77**, 061306 (2008).
- ²⁵R. Al-Raoush and A. Papadopoulos, "Representative elementary volume analysis of porous media using X-ray computed tomography," *Powder Technology* **200**, 69–77 (2010).
- ²⁶A. Gillman, K. Matouš, and S. Atkinson, "Microstructure-statistics-property relations of anisotropic polydisperse particulate composites using tomography," *Physical Review E* **87**, 022208 (2013).
- ²⁷C. Xia, Y. Cao, B. Kou, J. Li, Y. Wang, X. Xiao, and K. Fezzaa, "Angularly anisotropic correlation in granular packings," *Physical Review E* **90**, 062201 (2014).
- ²⁸K. Heim, F. Bernier, R. Pelletier, and L. P. Lefebvre, "High resolution pore size analysis in metallic powders by X-ray tomography," *Case Studies in Nondestructive Testing and Evaluation* **6**, 45–52 (2016).
- ²⁹V. Baranau, S.-C. Zhao, M. Scheel, U. Tallarek, and M. Schröter, "Upper bound on the Edwards entropy in frictional monodisperse hard-sphere packings," *Soft Matter* **12**, 3991–4006 (2016).
- ³⁰M. Scheel, R. Seemann, M. Brinkmann, M. Di Michiel, A. Sheppard, B. Breidenbach, and S. Herminghaus, "Morphological clues to wet granular pile stability," *Nature Materials* **7**, 189–193 (2008).
- ³¹E. Brown, A. Nasto, A. G. Athanassiadis, and H. M. Jaeger, "Strain Stiffening in Random Packings of Entangled Granular Chains," *Physical Review Letters* **108**, 108302 (2012).
- ³²Y. X. Cao, B. Chakraborty, G. C. Barker, A. Mehta, and Y. J. Wang, "Bridges in three-dimensional granular packings: Experiments and simulations," *Europhysics Letters* **102**, 24004 (2013).
- ³³G. W. Delaney, T. D. Matteo, and T. Aste, "Combining tomographic imaging and DEM simulations to investigate the structure of experimental sphere packings," *Soft Matter* **6**, 2992–3006 (2010).
- ³⁴M. Saadatfar, A. P. Sheppard, T. J. Senden, and A. J. Kabla, "Mapping forces in a 3d elastic assembly of grains," *Journal of the Mechanics and Physics of Solids* **60**, 55–66 (2012).
- ³⁵R. Hurley, S. Hall, J. Andrade, and J. Wright, "Quantifying Interparticle Forces and Heterogeneity in 3d Granular Materials," *Physical Review Letters* **117**, 098005 (2016).
- ³⁶S. Hall, M. Bornert, J. Desrues, Y. Pannier, N. Lenoir, G. Viggiani, and P. Bésuelle, "Discrete and continuum analysis of localised deformation in sand using X-ray μ CT and volumetric digital image correlation," *Géotechnique* **60**, 315–322 (2010).
- ³⁷E. Andò, S. A. Hall, G. Viggiani, J. Desrues, and P. Bésuelle, "Grain-scale experimental investigation of localised deformation in sand: a discrete particle tracking approach," *Acta Geotechnica* **7**, 1–13 (2012).
- ³⁸E. Andò, G. Viggiani, S. A. Hall, and J. Desrues, "Experimental micro-mechanics of granular media studied by x-ray tomography: recent results and challenges," *Géotechnique Letters* **3**, 142–146 (2013).
- ³⁹A. Tordesillas, D. M. Walker, E. Andò, and G. Viggiani, "Revisiting localized deformation in sand with complex systems," *Proc. R. Soc. A* **469**, 20120606 (2013).
- ⁴⁰R. Alikarami, E. Andò, M. Gkiousas-Kapnisis, A. Torabi, and G. Viggiani, "Strain localisation and grain breakage in sand under shearing at high mean stress: insights from in situ X-ray tomography," *Acta Geotechnica* **10**, 15–30 (2015).
- ⁴¹A. Hemmerle, M. Schröter, and L. Goehring, "A cohesive granular material with tunable elasticity," *Scientific Reports* **6**, 35650 (2016).
- ⁴²Y. Fu, Y. Xi, Y. Cao, and Y. Wang, "X-ray microtomography study of the compaction process of rods under tapping," *Physical Review E* **85**, 051311 (2012).
- ⁴³T. Börzsönyi, B. Szabó, G. Törös, S. Wegner, J. Török, E. Somfai, T. Bien, and R. Stannarius, "Orientational Order and Alignment of Elongated Particles Induced by Shear," *Physical Review Letters* **108**, 228302 (2012).
- ⁴⁴T. Börzsönyi, B. Szabó, S. Wegner, K. Harth, J. Török, E. Somfai, T. Bien, and R. Stannarius, "Shear-induced alignment and

- dynamics of elongated granular particles,” *Physical Review E* **86**, 051304 (2012).
- ⁴⁵S. Wegner, T. Börzsönyi, T. Bien, G. Rose, and R. Stannarius, “Alignment and dynamics of elongated cylinders under shear,” *Soft Matter* **8**, 10950–10958 (2012).
- ⁴⁶V. Yadav, J.-Y. Chastaing, and A. Kudrolli, “Effect of aspect ratio on the development of order in vibrated granular rods,” *Physical Review E* **88**, 052203 (2013).
- ⁴⁷S. Wegner, R. Stannarius, A. Boese, G. Rose, B. Szabó, E. Somfai, and T. Börzsönyi, “Effects of grain shape on packing and dilatancy of sheared granular materials,” *Soft Matter* **10**, 5157–5167 (2014).
- ⁴⁸G. Wortel, T. Börzsönyi, E. Somfai, S. Wegner, B. Szabó, R. Stannarius, and M. v. Hecke, “Heaping, secondary flows and broken symmetry in flows of elongated granular particles,” *Soft Matter* **11**, 2570–2576 (2015).
- ⁴⁹T. Börzsönyi, E. Somfai, B. Szabó, S. Wegner, P. Mier, G. Rose, and R. Stannarius, “Packing, alignment and flow of shape-anisotropic grains in a 3D silo experiment,” *New Journal of Physics* **18**, 093017 (2016).
- ⁵⁰T. Finger, M. Schröter, and R. Stannarius, “The mechanism of long-term coarsening of granular mixtures in rotating drums,” *New Journal of Physics* **17**, 093023 (2015).
- ⁵¹A. Schella, S. Herminghaus, and M. Schröter, “Influence of humidity on tribo-electric charging and segregation in shaken granular media,” *Soft Matter* **13**, 394–401 (2017).
- ⁵²N. Francois, M. Saadatfar, R. Cruikshank, and A. Sheppard, “Geometrical frustration in amorphous and partially crystallized packings of spheres,” *Physical Review Letters* **111**, 148001 (2013).
- ⁵³M. Hanifpour, N. Francois, S. Vaez Allaei, T. Senden, and M. Saadatfar, “Mechanical Characterization of Partially Crystallized Sphere Packings,” *Physical Review Letters* **113**, 148001 (2014).
- ⁵⁴M. Hanifpour, N. Francois, V. Robins, A. Kingston, S. M. Vaez Allaei, and M. Saadatfar, “Structural and mechanical features of the order-disorder transition in experimental hard-sphere packings,” *Physical Review E* **91**, 062202 (2015).
- ⁵⁵J. Li, Y. Cao, C. Xia, B. Kou, X. Xiao, K. Fezzaa, and Y. Wang, “Similarity of wet granular packing to gels,” *Nature Communications* **5**, 5014 (2014).
- ⁵⁶C. Xia, J. Li, Y. Cao, B. Kou, X. Xiao, K. Fezzaa, T. Xiao, and Y. Wang, “The structural origin of the hard-sphere glass transition in granular packing,” *Nature Communications* **6**, 8409 (2015).
- ⁵⁷B. Zhao, J. Wang, M. R. Coop, G. Viggiani, and M. Jiang, “An investigation of single sand particle fracture using X-ray micro-tomography,” *Géotechnique* **65**, 625–641 (2015).
- ⁵⁸probably on Dryad, only available after acceptance of manuscript.
- ⁵⁹R. Stannarius, “Magnetic resonance imaging of granular materials,” *Rev. Sci. Instr.* (2017), <https://arxiv.org/abs/1703.01211>.
- ⁶⁰J. A. Dijkstra, F. Rietz, K. A. Lőrincz, M. van Hecke, and W. Losert, “Invited Article: Refractive index matched scanning of dense granular materials,” *Review of Scientific Instruments* **83**, 011301–011301–12 (2012).
- ⁶¹R. B. Joshua Dijkstra, N. Brodu, “Refractive index matched scanning and detection of soft particles,” *Review of Scientific Instruments* (2017), <https://arxiv.org/abs/1703.02816>.
- ⁶²I. Vlahinić, E. Andò, G. Viggiani, and J. E. Andrade, “Towards a more accurate characterization of granular media: extracting quantitative descriptors from tomographic images,” *Granular Matter* **16**, 9–21 (2014).
- ⁶³R. Kawamoto, E. Andò, G. Viggiani, and J. E. Andrade, “Level set discrete element method for three-dimensional computations with triaxial case study,” *Journal of the Mechanics and Physics of Solids* **91**, 1–13 (2016).
- ⁶⁴I. Vlahinić, R. Kawamoto, E. Andò, G. Viggiani, and J. E. Andrade, “From computed tomography to mechanics of granular materials via level set bridge,” *Acta Geotechnica* , 1–11 (2016).
- ⁶⁵F. M. Schaller, M. Neudecker, M. Saadatfar, G. Delaney, K. Mecke, G. E. Schröder-Turk, and M. Schröter, “Tomographic analysis of jammed ellipsoid packings,” in *AIP Conference Proceedings*, Vol. 1542 (AIP Publishing, 2013) pp. 377–380.
- ⁶⁶F. M. Schaller, M. Neudecker, M. Saadatfar, G. W. Delaney, G. E. Schröder-Turk, and M. Schröter, “Local Origin of Global Contact Numbers in Frictional Ellipsoid Packings,” *Physical Review Letters* **114**, 158001 (2015).
- ⁶⁷F. M. Schaller, S. C. Kapfer, J. E. Hilton, P. W. Cleary, K. Mecke, C. D. Michele, T. Schilling, M. Saadatfar, M. Schröter, G. W. Delaney, and G. E. Schröder-Turk, “Non-universal Voronoi cell shapes in amorphous ellipsoid packs,” *Europhysics Letters* **111**, 24002 (2015).
- ⁶⁸<https://github.com/spatialfruitsalad/volume2position> (2017).
- ⁶⁹S.-C. Zhao, *Length scales in granular matter*, Ph.D. thesis, Georg-August-Universität Göttingen (2013), <http://hdl.handle.net/11858/00-1735-0000-0015-9D98-C>.
- ⁷⁰C. Kleinschmidt, “Analytical considerations of beam hardening in medical accelerator photon spectra,” *Medical Physics* **26**, 1995–1999 (1999).
- ⁷¹C. Tomasi and R. Manduchi, “Bilateral filtering for gray and color images,” in *Computer Vision, 1998. Sixth International Conference on* (IEEE, 1998) pp. 839–846.
- ⁷²N. Otsu, “A threshold selection method from gray-level histograms,” *Automatica* **11**, 23–27 (1975).
- ⁷³M. Neudecker, S. Ulrich, S. Herminghaus, and M. Schröter, “Jamming of frictional tetrahedra,” *Physical Review Letters*, **111**, 028001 (2013).
- ⁷⁴M. Neudecker, *Geometric structure and mechanical stability of disordered tetrahedra packings*, Ph.D. thesis, Georg-August-Universität Göttingen (2013), <http://hdl.handle.net/11858/00-1735-0000-0022-609B-9>.
- ⁷⁵T. Aste, M. Saadatfar, A. Sakellariou, and T. J. Senden, “Investigating the geometrical structure of disordered sphere packings,” *Physica A: Statistical Mechanics and its Applications* **339**, 16–23 (2004).
- ⁷⁶C. Xia, K. Zhu, Y. Cao, H. Sun, B. Kou, and Y. Wang, “X-ray tomography study of the random packing structure of ellipsoids,” *Soft Matter* **10**, 990–996 (2014).
- ⁷⁷L.-N. Zou, X. Cheng, M. L. Rivers, H. M. Jaeger, and S. R. Nagel, “The Packing of Granular Polymer Chains,” *Science* **326**, 408–410 (2009).
- ⁷⁸M. van Hecke, “Jamming of soft particles: geometry, mechanics, scaling and isostaticity,” *J. Phys.: Condens. Matter* **22**, 033101 (2010).
- ⁷⁹A. J. Liu and S. R. Nagel, “The jamming transition and the marginally jammed solid,” *Ann. Rev. Cond. Matt. Phys.* **1**, 347–369 (2010).
- ⁸⁰In a system of soft particles, this broadening might also be due to deformations of the particles.⁶¹
- ⁸¹J. Murison, R. Moosavi, M. Schulz, B. Schillinger, and M. Schröter, “Neutron Tomography as a Tool To Study Immiscible Fluids in Porous Media without Chemical Dopants,” *Energy & Fuels* **29**, 6271 (2015).
- ⁸²https://bitbucket.org/Laguna_999/raps (2017).
- ⁸³J. D. Bernal and J. Mason, “Co-ordination of randomly packed spheres,” *Nature* **188**, 910–911 (1960).
- ⁸⁴D. Pinson, R. P. Zou, A. B. Yu, P. Zulli, and M. J. McCarthy, “Coordination number of binary mixtures of spheres,” *Journal of Physics D: Applied Physics* **31**, 457 (1998).
- ⁸⁵J. Blouwolf and S. Fraden, “The coordination number of granular cylinders,” *Europhysics Letters* **76**, 1095–1101 (2006).
- ⁸⁶X.-D. Zhang, C.-J. Xia, X.-H. Xiao, and Y.-J. Wang, “Fast synchrotron x-ray tomography study of the packing structure of rods with different aspect ratios,” *Chin. Phys. B* **23**, 044501 (2014).
- ⁸⁷H. Makse, “Software and data: Research on hard sphere packings,” (2013), <http://www-levich.engr.cny.cuny.edu/webpage/hmakse/software-and-data/>.
- ⁸⁸<http://www.gnuplot.info> (2017).
- ⁸⁹N. N. Thyagu, M. Neudecker, and M. Schröter, “Local analysis of the history dependence in tetrahedra packings,” (2015), <https://arxiv.org/abs/1501.04472>.
- ⁹⁰F. Radjai, M. Nakagawa, and S. Luding, “Force and fabric states in granular media,” *AIP Conference Proceedings* **1145**,

- 35–42 (2009).
- ⁹¹R. Blumenfeld and S. F. Edwards, “Granular entropy: Explicit calculations for planar assemblies,” *Physical Review Letters* **90**, 114303 (2003).
- ⁹²C. Song, P. Wang, and H. A. Makse, “A phase diagram for jammed matter,” *Nature* **453**, 629–632 (2008).
- ⁹³J. G. Puckett, F. Lechenault, and K. E. Daniels, “Local origins of volume fraction fluctuations in dense granular materials,” *Phys. Rev. E* **83**, 041301 (2011).
- ⁹⁴A. Baule, R. Mari, L. Bo, L. Portal, and H. A. Makse, “Mean-field theory of random close packings of axisymmetric particles,” *Nature Comm.* **4**, 2194 (2013).
- ⁹⁵A. Baule and H. A. Makse, “Fundamental challenges in packing problems: from spherical to non-spherical particles,” *Soft Matter* **10**, 4423–4429 (2014).
- ⁹⁶M. Pica Ciamarra, “Comment on granular entropy: Explicit calculations for planar assemblies,” *Physical Review Letters* **99**, 089401 (2007).
- ⁹⁷F. W. Starr, S. Sastry, J. F. Douglas, and S. C. Glotzer, “What do we learn from the local geometry of glass-forming liquids?” *Physical review letters* **89**, 125501 (2002).
- ⁹⁸V. S. Kumar and V. Kumaran, “Voronoi cell volume distribution and configurational entropy of hard-spheres,” *J. Chem. Phys.* **123**, 114501 (2005).
- ⁹⁹T. Aste and T. Di Matteo, “Emergence of Gamma distributions in granular materials and packing models,” *Physical Review E* **77**, 021309 (2008).
- ¹⁰⁰R. F. Shepherd, J. C. Conrad, T. Sabuwala, G. G. Gioia, and J. A. Lewis, “Structural evolution of cuboidal granular media,” *Soft Matter* **8**, 4795–4801 (2012).
- ¹⁰¹V. Luchnikov, N. Medvedev, L. Oger, and J.-P. Troadec, “Voronoi-delaunay analysis of voids in systems of nonspherical particles,” *Physical review E* **59**, 7205 (1999).
- ¹⁰²E. Preteux, “Watershed and skeleton by influence zones: A distance-based approach,” *Journal of Mathematical Imaging and Vision* **1**, 239–255 (1992).
- ¹⁰³<http://theorie1.physik.fau.de/research/pomelo/index.html> (2017).
- ¹⁰⁴G. E. Schröder-Turk, W. Mickel, M. Schröter, G. W. Delaney, M. Saadatfar, T. J. Senden, K. Mecke, and T. Aste, “Disordered spherical bead packs are anisotropic,” *Europhys. Lett.* **90**, 34001–6 (2010).
- ¹⁰⁵G. E. Schröder-Turk, W. Mickel, S. C. Kapfer, F. M. Schaller, B. Breidenbach, D. Hug, and K. Mecke, “Minkowski tensors of anisotropic spatial structure,” *New Journal of Physics* **15**, 083028 (2013).
- ¹⁰⁶S. Alesker, “Description of continuous isometry covariant valuations on convex sets,” *Geometriae dedicata* **74**, 241–248 (1999).
- ¹⁰⁷S. C. Kapfer, W. Mickel, F. M. Schaller, M. Spanner, C. Goll, T. Nogawa, N. Ito, K. Mecke, and G. E. Schröder-Turk, “Local anisotropy of fluids using minkowski tensors,” *Journal of Statistical Mechanics: Theory and Experiment* **2010**, P11010 (2010).
- ¹⁰⁸S. C. Kapfer, W. Mickel, K. Mecke, and G. E. Schröder-Turk, “Jammed spheres: Minkowski tensors reveal onset of local crystallinity,” *Physical Review E* **85**, 030301 (2012).
- ¹⁰⁹W. Mickel, S. Münster, L. M. Jawerth, D. A. Vader, D. A. Weitz, A. P. Sheppard, K. Mecke, B. Fabry, and G. E. Schröder-Turk, “Robust pore size analysis of filamentous networks from three-dimensional confocal microscopy,” *Biophysical journal* **95**, 6072–6080 (2008).
- ¹¹⁰G. E. Schröder-Turk, S. Kapfer, B. Breidenbach, C. Beisbart, and K. Mecke, “Tensorial minkowski functionals and anisotropy measures for planar patterns,” *Journal of microscopy* **238**, 57–74 (2010).
- ¹¹¹A. G. Athanassiadis, M. Z. Miskin, P. Kaplan, N. Rodenberg, S. H. Lee, J. Merritt, E. Brown, J. Amend, H. Lipson, and H. M. Jaeger, “Particle shape effects on the stress response of granular packings,” *Soft Matter* **10**, 48–59 (2013).
- ¹¹²C. Scholz, S. D’Silva, and T. Pöschel, “Ratcheting and tumbling motion of Vibrots,” *New Journal of Physics* **18**, 123001 (2016).
- ¹¹³D. Wildenschild and A. P. Sheppard, “X-ray imaging and analysis techniques for quantifying pore-scale structure and processes in subsurface porous medium systems,” *Advances in Water Resources* **51**, 217–246 (2013).
- ¹¹⁴L. Leu, S. Berg, F. Enzmann, R. T. Armstrong, and M. Kersten, “Fast X-ray Micro-Tomography of Multiphase Flow in Berea Sandstone: A Sensitivity Study on Image Processing,” *Transport in Porous Media* **105**, 451–469 (2014).
- ¹¹⁵M. Andrew, H. Menke, M. J. Blunt, and B. Bijeljic, “The Imaging of Dynamic Multiphase Fluid Flow Using Synchrotron-Based X-ray Microtomography at Reservoir Conditions,” *Transport in Porous Media* **110**, 1–24 (2015).
- ¹¹⁶<http://datadryad.org/> (2017).
- ¹¹⁷<https://zenodo.org/> (2017).
- ¹¹⁸Tal Yarkoni, <https://twitter.com/talyarkoni/status/767419633527689216> (2016).
- ¹¹⁹<http://fiji.sc/> (2017).
- ¹²⁰<http://www.theorie1.physik.uni-erlangen.de/research/karambola/> (2017).
- ¹²¹<http://fiji.sc/> (2017).
- ¹²²To find out the amount of memory available to Fiji, check the settings in *Edit* → *Options* → *Memory and Threads*.
- ¹²³<http://math.lbl.gov/voro++/> (2017).
- ¹²⁴C. Rycroft, “Voro++: A three-dimensional Voronoi cell library in C++,” Lawrence Berkeley National Laboratory (2009).
- ¹²⁵J. Hoshen and R. Kopelman, “Percolation and cluster distribution. i. cluster multiple labeling technique and critical concentration algorithm,” *Physical Review B* **14**, 3438 (1976).

Appendix A: Analyzing the example volume dataset

This appendix lists in a concise way all the steps necessary to analyze the example data set accompanying this paper.

1. Obtaining code and data

- Download the example volume from⁵⁸ and store it as `volume.raw` in your working directory. This volume file has been acquired with a Nanotom Tomograph from *GE Sensing and Inspection*. Imaging conditions were 120 kV, 120 μ A with 6 averages, each with an exposure time of 250 ms and a total of 1400 projections. The original volume had a size of $1132 \times 1132 \times 1152$ voxels. After binning and cropping, the volume was reduced to a total of $512 \times 512 \times 512$ voxels. The sample consists of spheres of POM with an diameter of 3.5 mm that have been tapped 16000 times with a maximum acceleration of $\Gamma = 2g$ at a frequency of 3 Hz.
- For viewing the volume file, download and install Fiji from the official web site.¹¹⁹
- The program `volume2positionList` is needed to extract a list of particle positions from the tomogram. The preferred way to obtain it is to download the source code from⁶⁸ and store in a sub folder `code` in your working folder. To compile the program, change to the code directory and call `make` there.
- While compiling `volume2positionList` from the source code should be considered the best option, we do understand that this might create an additional barrier for some users. Therefore we provide as an alternative a static linked binary with the supplemental material. It should run out of the

box on most 64-Bit Linux PC's. The supplemental material contains also static linked binaries for the other three analysis programs discussed below.

5. To calculate the pair correlation function and the global contact number, you will need to download the source code for the program `raps` from⁸² and store it into a folder called `raps` in the working directory. `raps` can be compiled with the included `build.bsh` shell script. For further instructions please refer to the included `README.md`.
6. Calculating the Set Voronoi diagrams, requires the program `pomelo`. The corresponding source code can be downloaded from¹⁰³ and then stored in folder called `pomelo` within the working directory. In order to compile `pomelo` with the included makefile, a compiler that supports most C++11 features is required, e.g. `clang++ 3.5.0-10`. Further information about compiling `pomelo` and the included examples are given in the file `README.md`.
7. If you want to characterize the Voronoi volumes using Minkowski tensors, you will need to download `karambola` from¹²⁰. After storing it in a folder called `karambola`, you can compile it with the included makefile.

2. Visualization using Fiji

Fiji is an image processing package that is built on top of ImageJ,¹²¹ an open source image processing program. Fiji is run in an java virtual machine. On some systems, the virtual machine starts with a limited amount of memory which is not enough for most 3D image applications.¹²² To tell the machine to use more memory a command line command has to be typed prior to starting Fiji. The following command will increase the memory limit to 2000MB, which is sufficient for the applications explained in this document.

```
export _JAVA_OPTIONS="-Xmx2000M -Xms2000M"
```

After that, start Fiji from the same command line.

To open a tomography file, you have to specify a number of parameters in the *open raw* dialogue. The parameters for the sample tomogram are given in figure 1 b). These parameters can be divided into three different groups: volume specific, visualisation choices and machine specific. The values for the sample data are given in square brackets.

The volume specific parameters are *Width*, *Height* and *Number of Images*. These parameters depend on both the settings which the tomography was taken with (size in x , y and z) and the choices made during the reconstruction of the tomogram. This information is typically contained in a text file saved together with the volume file. Or it can be obtained from the export dialog for the volume in the reconstruction software. [use 512 for each dimension] Machine specific parameters will be identical for all volumes exported from the same reconstruction software and should be documented in the manual belonging to that software:

Image Type: The data type of the individual voxels are stored in. [16-Bit Unsigned]

Offset: Size of a possible header preceding the volume data (in bit). Use 0 for none. [0]

Gap: Size of a possible header preceding each slice (in bit). Use 0 for none. [0]

Byte Order: Integers can be stored in two different ways. This switch reverses the order of the binary values of each datatype. [Check]

Open All Files: Some software saves the volume not as one single file but as series of multiple files (e.g. the different slices of a tomogram). This option will load all of them. [Uncheck]

Finally, there are two choices which influence how the volume is visualized:

White is zero: In x-ray tomographies the value of a voxel is proportional to the local absorption coefficient: white corresponds to high absorption. This switch would invert this relationship. [Uncheck]

Use virtual Stack: 3D volume dataset can become several GByte large. If a PC has not enough RAM to load the complete image data instantly to the memory, this switch allows to just load the slice which is presently accessed for viewing or processing. This option has a serious impact on performance. [Uncheck]

3. Particle detection on the example data

The program `volume2positionList` identifies all spheres in the volume data set (using the methods described in section III) and then exports their particle positions as a text file. The parameters of `volume2positionList` are [inFileName] [outFolderName] [nx] [ny] [nz] [erosion depth] [sigma_g] [sigma_p].

The parameters `inFileName` and `outFolderName` must be adapted to your filesystem structure. `nx`, `ny`, `nz` are the size of the volume file (512 for the example). `erosion depth` refers to the erosion step described in section III B and should be set to a value of 5 voxels. The `sigma` parameters correspond to the respective values in the bilateral filter step σ_g and σ_p .

All output will be written to the output folder `outFolderName`. The program will also create a subdirectory `images` which contains slices at three different heights through the volume at different processing steps. The list of particle positions will be written to a file called `particles_centroids_ed5.dat`. To run the program on the example data, use

```
volume2positionList volume.raw output 512 512
                    512 5 1.75 2000
```

After running `volume2positionList`, the first two lines of `particles_centroids_ed5.dat` in the the analysis directory should look like this:

```
255.106 255.061 255.083 0 90197774
345.993 190.616 38.1658 472 10746
```

The first line represents the air cluster, the second line gives the coordinates (column number 1 to 3) of the first detected sphere. Column 4 lists the id of the particles, column 5 is the volume of the particle.

4. Pair correlation calculation with raps

The program `raps` receives its parameters by loading a `data.set` file. For our example this file has to contain the following line:

```
particles_centroids_ed5.dat ip_example 0.005
27.17.
```

The first entry is the filename of the position list, the second entry an identifier that will be used to label the output files. The number in the third column is the bin size Δr (cf. equation 3) used for computing the pair correlation function. The last number is the particle diameter, which is needed to compute the raw data used in the CNS function fit described in the next section. The value of 27.17 is the correct particle diameter for the demo data; for other raw data you should provide an educated guess which can then be updated in a second iteration once you have measured the particle diameter as described in the next section.

After creating the the configuration file `data.set` you can call the program (from the analysis folder) with the command

```
../raps/RAPS data.set.
```

`raps` will calculate structural properties of the packing, such as the numerator in equation (3), the pair correlation function $g(r)$ (`pc_ip-example.dat`) (the normalisation has to be performed by the user) and the raw data required to compute the contact number (`cns_ip_example.dat`). Each file will contain information how to plot it using `gnuplot`.⁸⁸

Computing the mean diameter of the particles is the first step in the next section and is described there.

5. Determining global contact numbers

Determining the global contact number using the ensemble based method, as described in section VA, is a two step process. While you can use any program capable of fitting equations to data to perform this task, we provide for convenience a `gnuplot`⁸⁸ skript named `find_contacts.plt` in the supplemental materials. Please note that fit-programs such as `gnuplot` normally use a standard Levenberg-Marquardt algorithm. Which means that the starting values for the fit parameters have to be chosen carefully, as the algorithm can easily get stuck in a erroneous, local minimum.

The first step is to compute the mean particle diameter by fitting the first peak of the pair correlation function with a Gaussian distribution. You will find the raw data of the pair correlation function in the file `pc_ip-example.dat` written by `raps`. The width of the

fitting window should be limited to include only the upper half of the first peak of $g(r)$. Fitting the $g(r)$ values of our demo dataset provides a mean sphere diameter d_{mean} of 27.177 voxels (cf. figure 6a).

The second step is to fit the contact number scaling function in equation 4 to the data in the file `cns_ip_example.dat`. First you should only determine the width of the error function σ by fitting $C(x)$ to the left part of the data, i.e. all points smaller than d_{mean} . This requires a reasonable estimate for Z . Our fit yields $\sigma = 0.0569$. Then the full CNS function can be fitted to determine the contact number Z (and the pre factor of the linear offset). The upper range of this fit should be chosen as the real particle diameter plus 5 times the width of the error function. The contact number of our demo dataset is 5.4.

6. Set Voronoi calculation on sphere packings

`pomelo` is a open source program, licensed under GPLv3 that uses the `vorop++` library (licensed under a modified BSD license).^{123,124} `pomelo` can be used to calculate the Set Voronoi cells from a list of sphere centers. The parameters are: `pomelo -mode SPHERE -i [inFileName] -o [outFolderName]`. In this command, `-i inFileName` should be the path to the `particles_centroids_ed5.dat` file created by `volume2positionList` program and `-o outFolderName` should be the path to the output folder. Note that for monodisperse spheres (`-mode SPHERE`) the Voronoi and the Set Voronoi diagram are identical. Thus it is sufficient to use the centers of each sphere to create the Voronoi Diagram. The command (out of the analysis folder) to run `pomelo` on the example data is

```
../pomelo/bin/pomelo -mode SPHERE -i
particles_centroids_ed5.dat -o pomeloOut
```

`pomelo` creates by default five files in the output folder. The file `reduced.xyz` contains the vertices, faces and cells of the Set Voronoi cells, the file `surface_triangulation.xyz` contains the surface of the particle, or in case of spheres, where the Set Voronoi cells coincide with the normal Voronoi cells, the centers of the particles. Both files can be plotted with `gnuplot` using `splot "surface_triangulation.xyz" u 2:3:4 w p` or `splot "reduced.xyz" u 2:3:4 w lp`

The files `cell.poly` and `cell.off` contain the same information as the file `surface_triangulation.xyz` but are intended to be used with `karambola` (`cell.poly`) and `geomview` (`cell.off`).

Finally, the file `setVoronoiVolumes.dat` contains the volume of each (Set) Voronoi cell. This information can be used to calculate the local packing fraction.

7. Calculate the Minkowski Tensors of the Set Voronoi cells

The Minkowski tensors and their Eigenvalues of the Set Voronoi cells can be calculated by the program

`karambola` using the output of `pomelo` (see section VIB) as input file. The necessary command (from the `pomeloOut` folder) is:

```
../../karambola/karambola -i cell.poly -o
karambolaOut -labels -reference_centroid
```

The parameters of `karambola` are the path to the poly file created by `pomelo` (`-i [input poly file]`), the output folder (`-o [output folder]`), and the the switch `-labels` which tells `karambola` to use the labels of the individual cells. Otherwise all cells would be combined into one large cell. The `-reference_centroid` option tells `karambola` to use the centroid of the cell as the reference point, in contrast to the default behavior where the origin of the sample will be used as the reference for calculating the Minkowski Tensors.

`Karambola`'s output consists of multiple files. The file `w000_w100_w200_w300` for example contains the information about the volume $W_0^{0,0}$, the surface area $W_1^{0,0}$, integral mean curvature $W_2^{0,0}$ and the integral Gaussian curvature (genus) $W_3^{0,0}$ of each Set Voronoi cell. With the particle volume $W_0^{0,0}$, the local packing fraction of each particle can be calculated. The file `w020_eigsys` contains the Eigenvalues and corresponding Eigenvectors of the $W_0^{2,0}$ Minkowski Tensor for each of the cells.

Appendix B: The Hoshen Kopelman algorithm

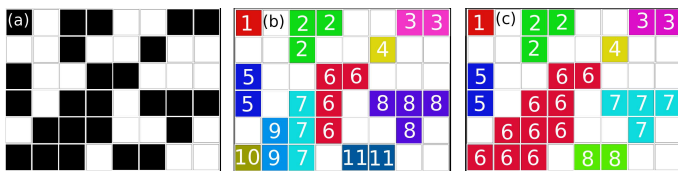


FIG. 12. Applying the Hoshen Kopelman algorithm on a two-dimensional binary image. (a) binarized image. (b) first step of the algorithm, before resolving the indirections. (c) final, labeled image.

Clusters of pixels or voxels can be identified with the HOSHEN KOPELMAN algorithm.¹²⁵ Figure 12 explains it on a two-dimensional image where we assume that the clusters are composed of black pixels. The algorithm iterates through all pixels of the binary image (figure 12(a)) starting at the top left corner and processing line by line from left to right. If the pixel under consideration is a white pixel, the algorithm proceeds to the next pixel. When a black pixel is encountered, it is assigned a cluster id which is determined by considering the left and top neighbor of that pixel, which have both already been visited by the algorithm.

If both are white pixels or pixels outside the image boundary, a new cluster id is assigned to the pixel under consideration. This is e.g. the case for pixel with cluster id 4 in figure 12(b), respectively the top pixel of cluster number 5. If either the left or the top neighbor is black, the cluster id of this pixel is used. An example is the first black pixel in row 2 which is assigned the cluster id of 2 stemming from the pixel above it. If both left and top

pixel are black, the lower of the cluster IDs of the neighbors is used as it is the case for the second black pixel in the lowest row of figure 12(b). All touching Clusters with different IDs are detected in this step and connectivity is stored.

Then in a second step, connected clusters are merged using the connectivity information. In this case, the clusters with IDs 6, 7, 9, 10 are all assigned value 6. The final labeled image is shown in figure 12(c).